

Universal conditional distribution function of [O II] luminosity of galaxies, and prediction for the [O II] luminosity function at redshift $z < 3$

HONGYU GAO¹ AND Y.P. JING^{1,2}

¹*Department of Astronomy, School of Physics and Astronomy, Shanghai Jiao Tong University, Shanghai 200240, People's Republic of China*

²*Tsung-Dao Lee Institute, and Shanghai Key Laboratory for Particle Physics and Cosmology, Shanghai Jiao Tong University, Shanghai 200240, People's Republic of China*

(Received XXX; Revised YYY; Accepted ZZZ)

Submitted to ApJ

ABSTRACT

The star-forming emission line galaxies (ELGs) with strong [O II] doublet are one of the main spectroscopic targets for the ongoing and upcoming fourth generation galaxy redshift surveys. In this work, we measure the [O II] luminosity $L_{[\text{O II}]}$ and the near-ultraviolet band absolute magnitude M_{NUV} for a large sample of galaxies in the redshift range of $0.6 \leq z < 1.45$ from the Public Data Release 2 (PDR-2) of the VIMOS Public Extragalactic Redshift Survey (VIPERS). We aim to construct the intrinsic relationship between the $L_{[\text{O II}]}$ and M_{NUV} through Bayesian analysis. In particular, we develop two different methods to properly correct for the incompleteness effect and observational errors in the [O II] emission line measurement. Our results indicate that the conditional distribution of $L_{[\text{O II}]}$ at a given M_{NUV} can be well described by a universal probability distribution function (PDF), which is independent of M_{NUV} or redshift. Convolution of the $L_{[\text{O II}]}$ conditional PDF with the NUV Luminosity function (LF) available in the literature, we make a prediction for [O II] LFs at $z < 3$. The predicted [O II] LFs are in good agreement with the observational results from the literature. Finally, we utilize the predicted [O II] LFs to estimate the number counts of [O II] emitters for the Subaru Prime Focus Spectrograph (PFS) survey. This universal conditional PDF of $L_{[\text{O II}]}$ provides a novel way to optimize the source targeting strategy for [O II] emitters in future galaxy redshift surveys, and to model [O II] emitters in theories of galaxy formation.

Keywords: Emission line galaxies (459), Luminosity function (942), Redshift surveys (1378), Dark energy (351)

1. INTRODUCTION

Understanding the accelerating expansion of the Universe is a central challenge for modern cosmology. In the current standard cosmological model, dark energy, which is introduced as a new form of energy, is thought to be responsible for the acceleration of the cosmic expansion. As powerful cosmological probes, the baryon acoustic oscillation (BAO, e.g., Cole et al. 2005; Eisenstein et al. 2005) and the redshift space distortion (RSD, e.g., Kaiser 1987) are expected to put tight constraints

on the dark energy model as well as to test gravity theories through measuring the Hubble expansion rate and the structure growth rate respectively. Both probes require a sufficient number of galaxies with redshift in a large cosmic volume in order to minimize statistical errors. Making such a redshift survey is the goal of ongoing Stage-IV projects such as the Dark Energy Spectroscopic Instrument (DESI, DESI Collaboration et al. 2016), the Subaru Prime Focus Spectrograph (PFS, Takada et al. 2014), 4-metre Multi-Object Spectroscopic Telescope (4MOST, de Jong et al. 2019), Euclid (Lau-reijs et al. 2011) and Wide Field Infrared Survey Telescope (WFIRST, Green et al. 2012; Spergel et al. 2015).

For the purpose of studying the dark energy at medium and high redshifts, emission line galaxies

(ELGs) whose spectra show significant emission line features are chosen as the primary targets for the redshift surveys. Among the emission lines commonly seen in galaxy spectra such as $H\alpha$ ($\lambda 6563$), [O III] ($\lambda 4959, \lambda 5006$), $H\beta$ ($\lambda 4861$) and [O II] ($\lambda 3726, \lambda 3729$), the forbidden [O II] line is one of the most prominent spectral lines because of its pronounced doublet shape, its strength, and its blue location in the rest-frame. For instance, DESI (DESI Collaboration et al. 2016) plans to target a large number of ELGs with strong [O II] flux in $0.6 < z < 1.6$ to achieve a high surface density of 2400 deg^{-2} , while PFS (Takada et al. 2014) aims to observe [O II] emitters in $0.8 < z < 2.4$ spanning a comoving volume $\sim 9 (\text{Gpc}/h)^3$. Before the spectroscopic observation, the [O II] emitter candidates will be pre-selected based on their photometric properties. In addition, the [O II] emission line is also an important indicator for the star formation rate (SFR) especially at high redshift (e.g., Kennicutt 1998; Kewley et al. 2004; Moustakas & Kennicutt 2006). Therefore, the [O II] luminosity function (LF), which describes the volume number density of [O II] emitters in a given luminosity bin, plays a significant role in effectively planning the future ELGs surveys and studying the theory of galaxy formation. In the last two decades, through both the spectroscopic observations and narrow-band imaging, the [O II] LF has been measured at different redshift (e.g., Gallego et al. 2002; Hippelein et al. 2003; Teplitz et al. 2003; Rigopoulou et al. 2005; Ly et al. 2007; Takahashi et al. 2007; Argenge & Lamareille 2009; Zhu et al. 2009; Gilbank et al. 2010; Bayliss et al. 2011; Sobral et al. 2012, 2013, 2015; Ciardullo et al. 2013; Drake et al. 2013; Comparat et al. 2015, 2016; Khostovan et al. 2015; Hayashi et al. 2018; Saito et al. 2020), though the determination remains very uncertain at redshift $z > 1.5$.

Motivated by making a precise forecast for the expected number density of [O II] emitters, predicting the [O II] LF as well as its redshift evolution is the main goal of this study. In the last five years, a series of observational studies have been carried out to measure the LF not only for the [O II] line but also for other emission lines. For instance, Mehta et al. (2015) develop the $H\alpha$ -[O III] bivariate line luminosity function for the ELGs data of the WFC3 Infrared Spectroscopic Parallel Survey (WISP, Atek et al. 2010, 2011), and predict the $H\alpha$ LF at $z \sim 2$ using [O III] emitters. Also for the $H\alpha$ emission line, Pozzetti et al. (2016) constructed three empirical models that can be used to estimate $H\alpha$ LF at given redshift. Using the multi-color photometry sample, Valentino et al. (2017) predict the $H\alpha$, $H\beta$, [O II] and [O III] line flux based on their SFR, stellar mass and some empirical recipes in order to compute the

number counts for these ELGs. De Barros et al. (2019) connect the [O III] + $H\beta$ flux with UV luminosity, and use this relation to predict [O III] + $H\beta$ LF at $z \sim 8$. Recently, Saito et al. (2020) model the emission-line flux for $H\alpha$ and [O II] by extracting information from the galaxy spectral energy distribution (SED) and then predict their number counts in the up-coming WFIRST and PFS surveys. Moreover, in addition to these observational studies, simulation and semi-analytic models (SAM) are also used to predict the emission line LFs (e.g., Park et al. 2015; Merson et al. 2018; Zhai et al. 2019; Favole et al. 2020). Particularly, Favole et al. (2020) investigate the linear scaling relations between [O II] luminosity and other global galactic properties including SFR, age, stellar mass, u and g band magnitude and use these proxies to estimate the [O II] LF.

In view of the fact that young, massive stars tend to produce intense UV radiation that can photo-ionize neutral oxygen atoms in the ionized regions (e.g., Oesterbrock 1974; Draine 2011), the [O II] emission line should be directly and tightly related with UV radiation. Accordingly, in this study, we attempt to construct the intrinsic relationship between the [O II] luminosity $L_{[\text{O II}]}$ and near-ultraviolet (NUV) band absolute magnitude M_{NUV} using a large number of emission line galaxies from the VIMOS Public Extragalactic Redshift Survey (VIPERS¹, Guzzo et al. 2014; Garilli et al. 2014; Scodreggio et al. 2018). Compared with the previous studies, we have paid our special attention to the incompleteness of faint [O II] emitters in the observation. The incompleteness changes with the intrinsic line strength and with the redshift. We develop a statistical model to characterize this relation and derive its parameters from our sample with two different methods that properly correct the incompleteness effect. We find that after the incompleteness is properly corrected for, the intrinsic relation between the [O II] line and the NUV rest-frame magnitude is universal for galaxies across the redshift between 0.6 and 1.1. With this universal relation, we predict the [O II] LFs from NUV LFs at redshift $z < 3$, and find that our predicted [O II] LFs are broadly in good agreement with observed [O II] LFs in the literature, though the observed ones still have large uncertainties. The intrinsic relation will also be very useful for theoretically understanding the formation of [O II] lines in galaxies.

This paper is arranged as follows. We first introduce the observational data set and the [O II] flux measurement in Section 2. Then we illustrate the model and fitting approach in Section 3. The main results and

¹ <http://vipers.inaf.it>

the prediction of [O II] LF are presented in Section 4. Finally, we make a summary in Section 5. The cosmological parameters assumed throughout the paper are $\Omega_{\Lambda,0} = 0.7$, $\Omega_{m,0} = 0.3$ and $H_0 = 70 \text{ km s}^{-1} \text{ Mpc}^{-1}$ at $z = 0$.

2. DATA

In this section, we briefly introduce the galaxy samples used in this study. The [O II] emission line fluxes and near-ultraviolet band absolute magnitudes M_{NUV} of these galaxies are measured through analyzing the spectroscopic data and multi-band photometric data, respectively.

2.1. VIPERS

The galaxy sample is selected from the second data release (Scodreggio et al. 2018) of the VIMOS Public Extragalactic Redshift Survey (VIPERS), which provides measured spectra for ~ 90000 objects in two fields (W1 and W4) of the Canada-France-Hawaii Telescope Legacy Survey Wide (CFHTLS-Wide²). The spectroscopic observations were carried out by the VIMOS multi-object spectrograph (Le Fèvre et al. 2003) attached on the ESO Very Large Telescope (VLT). The spectra span wavelength $5500 - 9500 \text{ \AA}$ with moderate resolution ($R \simeq 220$). Combining their own WIRCam observation with the photometric data from T0007³ release of the CFHTLS Wide photometric survey, GALEX (Martin et al. 2005), and the VISTA Deep Extragalactic Observations (Jarvis et al. 2013), Moutard et al. (2016) constructed a multi-band photometric catalog for the VIPERS sky footprints, called VIPERS Multi-Lambda Survey, that includes photometry at two UV bands NUV and FUV, five optical bands u, g, r, i, z, and one Near-IR bands K_s or K_{video} (only for part of W1).

We need to take into account the observational effects of the VIPERS observation. Following their notions, we can decompose the observational effects of VIPERS into radial selection function and angular selection function. Firstly, the radial selection function is induced by the color target pre-selection which aims to ensure that only galaxies with redshift greater than 0.5 are included in the parent photometric sample. This effect can be quantified by the color sampling rate (CSR) which was estimated by Guzzo et al. (2014) as a function of redshift. At $z < 0.6$, CSR can be modeled as $CSR(z) = 1/2 - 1/2 \text{erf}[b(z_t - z)]$ where the erf is the error function, and $b = 10.8$ and $z_t = 0.444$ are the best-fit parameters. At $z \geq 0.6$, the survey is highly

complete for $i_{\text{AB}} < 22.5$ (i.e. $CSR(z) = 1$). As for the angular selection function, in addition to the photometric and spectroscopic masks, the target sampling rate (TSR) and the spectroscopic success rate (SSR) have been evaluated for each galaxy (Scodreggio et al. 2018). The former is the probability that a galaxy in the parent sample is selected for the spectroscopic observation, and the latter accounts for the probability that the spectrum was successfully obtained. Therefore, we weight every galaxy by the inverse of CSR , TSR and SSR

$$w^i = CSR^{-1} \times TSR^{-1} \times SSR^{-1}. \quad (1)$$

Nevertheless, as the strength of an [O II] emitter depends on the color, the intrinsic relation between [O II] and NUV may be biased by the target color selection. Therefore, we restrict the galaxy sample in the range of $0.6 \leq z < 1.45$ to ensure that $CSR(z) = 1$. Finally, only galaxies with secure redshift determination (i.e. redshift flags 2 to 9; Scodreggio et al. 2018) are used in our study.

2.2. Measurement of $L_{[\text{O II}]}$ and M_{NUV}

The flux has been fully calibrated for the spectra of VIPERS galaxies (Garilli et al. 2014), thus we can directly use these cleaned-spectra without extra correction for slit losses. For each galaxy spectrum, we first shift it to the rest-frame and then mask the pixels in the region centered at 3727 \AA with width $\pm 20 \text{ \AA}$, which accounts for the broadening of spectral line caused by the resolution $R = 220$ of VIMOS spectrograph. The continuum is estimated by a sixth-order polynomial fitting in the range of $3727 \pm 200 \text{ \AA}$. After subtracting the continuum from the original spectra, we model the [O II] doublet by a single Gaussian profile rather than two Gaussian functions because of the limited spectrum resolution. We use the Levenberg-Marquardt algorithm (Levenberg 1944; Marquardt 1963) which is an optimized least squares method to fit the subtracted spectrum and derive the best-fitting parameters as well as their covariance matrix. The flux of the [O II] emission line $F_{[\text{O II}]}$ is obtained from the best-fitting Gaussian profile, and its measurement uncertainty is estimated from the covariance matrix. In APPENDIX A, we check our [O II] measurement method, by applying it to the spectra from the VIMOS VLT Deep Survey (VVDS, Le Fèvre et al. 2005, 2013) and comparing our results with the [O II] flux provided by Lamareille et al. (2009). There is a small systematic difference (less than 10%) between the two measurements, maybe due to the fact that they used a different method for the continuum fitting. Nevertheless, the two measurements agree well overall, and this slight difference does not significantly affect our subsequent conclusions. By applying our method to a total of

² <http://www.cfht.hawaii.edu/Science/CFHLS/>

³ <http://www.cfht.hawaii.edu/Science/CFHLS/T0007/>

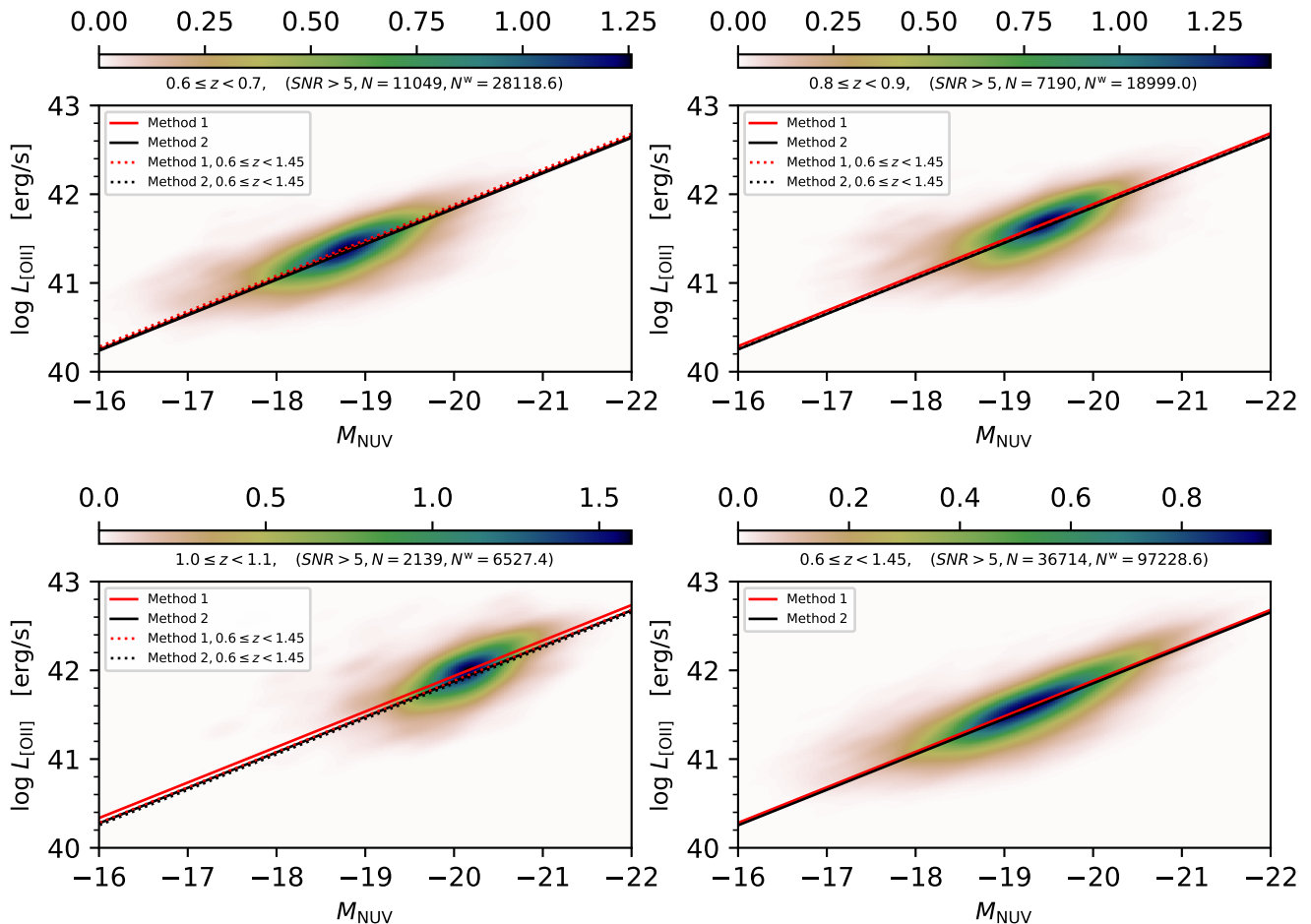


Figure 1. Two-dimensional joint probability distribution function (PDF) of $\log L_{[\text{O II}]}$ and M_{NUV} . Only galaxies with the $L_{[\text{O II}]}$ signal to noise ratio (SNR) greater than five are included. The color bar shows the value of the PDF at each pixel, which is calculated based on the kernel density estimate (KDE) with a Gaussian kernel. The first three panels display the PDF in different redshift bins and the last one presents that in the range of $0.6 \leq z < 1.45$. The number N and weighted number N^w of the galaxies used are also shown in the title of each panel. The red (method 1) and black (method 2) lines, which often overlap each other, represent the expectation values $\log L_{[\text{O II}]}^{\text{exp}}$ at which the PDF of $L_{[\text{O II}]}$ reaches the maximum at given M_{NUV} in the model (cf. Section 3.1). The $\log L_{[\text{O II}]}^{\text{exp}}$ is numerically calculated via Equation 6 and Equation 7 with our best-fit parameters shown in Table 1. Meanwhile, the $\log L_{[\text{O II}]}^{\text{exp}}$ of the last panel is also plotted as the dotted lines in the first three panels, which show little evolution of the $L_{[\text{O II}]}$ - M_{NUV} intrinsic relation over the redshift range probed.

54166 galaxies with the redshift flag ≥ 2 in the VIPERS sample, eventually we have detected the [O II] flux for 45139 galaxies (i.e. $F_{[\text{O II}]} > 0$ with the error successfully calculated, see APPENDIX A for more details), of which 36714 have signal to noise ratios (SNR) higher than 5.

We correct the $F_{[\text{O II}]}$ for the foreground dust extinction of the Milky Way by

$$F_{[\text{O II}]}^{\text{cor}} = F_{[\text{O II}]} \times 10^{0.4E(B-V)k(\lambda_{[\text{O II}]})}, \quad (2)$$

where $E(B-V)$ is the color excess taken from the dust map provided by Schlegel et al. (1998), and the $k(\lambda)$ is the reddening curve from Calzetti et al. (2000). Then,

we calculate [O II] luminosity $L_{[\text{O II}]}$ utilizing

$$L_{[\text{O II}]} = 4\pi F_{[\text{O II}]}^{\text{cor}} D_L^2, \quad (3)$$

where D_L is the luminosity distance defined as

$$D_L(z) = (1+z) \frac{c}{H_0} \int_0^z \frac{dz'}{\sqrt{\Omega_{m,0}(1+z')^3 + \Omega_{\Lambda,0}}}. \quad (4)$$

Simultaneously, utilizing the eight-band photometric data from the VIPERS Multi-Lambda Survey, we perform spectral energy distribution (SED) template fitting using LE PHARE (Arnouts et al. 2002; Ilbert et al. 2006) to all galaxies and derive their near-ultraviolet band absolute magnitudes M_{NUV} as well as other physical parameters such as stellar mass, age and SFR. In

our SED fitting, the stellar population synthesis models are taken from the library provided by Bruzual & Charlot (2003) and the Chabrier (2003) initial stellar mass function is adopted. We set three metallicities $0.4Z_{\odot}$, $1Z_{\odot}$ and $2.5Z_{\odot}$ and consider a delayed star formation history (SFH) $\sim t \exp(-t/\tau)$ where the timescale τ uniformly spans in the logarithm space from 10^7 yr to 1.258×10^{10} yr. As for the dust extinction, the color excess $E(B - V)$ is taken from 0 to 0.5 and the starburst reddening curve (Calzetti et al. 2000) is applied to calculate the attenuation factor.

Figure 1 shows the two-dimensional joint probability density distribution (PDF) of M_{NUV} and $\log L_{[\text{O II}]}$ for galaxies with $SNR > 5$ in different redshift bins. The color bars display the value of this joint PDF that is calculated based on the kernel density estimate (KDE) with a Gaussian kernel. Clearly, the intensity of [O II] is tightly correlated with M_{NUV} . This phenomenon is expected, as galaxies with stronger UV radiation are more likely to photo-ionize neutral oxygen and produce stronger [O II] emission line.

3. INTRINSIC CONDITIONAL DISTRIBUTION FUNCTION

In this section, we will describe the methods we use to model the intrinsic conditional probability density distribution $p^{\text{int}}(L_{[\text{O II}]}|M_{\text{NUV}})$ from the observational data. We note that because of the given sensitivity, the observation may fail in yielding a [O II] line detection for a relatively weaker emitter. This incompleteness depends on the strength and on the redshift of the emitters. We will pay particular attention to the incompleteness effect of the [O II] emission line measurement. Two methods are adopted to overcome the observational effects, and, as will be shown, produce similar results.

3.1. Intrinsic model

When predicting [O II] LF from the NUV LF, the most critical step is to derive the intrinsic relation between $L_{[\text{O II}]}$ and M_{NUV} .

As shown in Figure 1, the mean relationship of M_{NUV} and $\log L_{[\text{O II}]}$ can be reasonably described via a linear model. Additionally, at a given M_{NUV} , the dispersion of the $\log L_{[\text{O II}]}$ distribution is less than 1 dex. Considering the above two factors, we attempt to construct a linear model plus a skew-normal distribution (O’Hagan & Leonard 1976) for $p^{\text{int}}(L_{[\text{O II}]}|M_{\text{NUV}})$ that can be expressed as

$$p^{\text{int}}(L_{[\text{O II}]}|M_{\text{NUV}}) = \frac{2}{\omega} \phi\left(\frac{\log L_{[\text{O II}]} - \xi}{\omega}\right) \times \Phi\left(\alpha \left(\frac{\log L_{[\text{O II}]} - \xi}{\omega}\right)\right), \quad (5)$$

where $\phi(x) = \frac{1}{\sqrt{2\pi}} e^{-\frac{x^2}{2}}$ denote the standard normal PDF and $\Phi(x) = \int_{-\infty}^x \phi(t) dt$ is defined as the cumulative distribution function (CDF). The parameter α ($\alpha = 0$ for a normal distribution) and ω describe the skewness and scale of the skew-normal PDF respectively, the location parameter $\xi = kM_{\text{NUV}} + b$ indicates the linear relation between M_{NUV} and $\log L_{[\text{O II}]}$. It should be noticed that the location parameter ξ is different from the location ξ_{max} where the PDF reaches the maximum value. The latter is defined as the mode of this distribution and can also be regarded as the expectation value of $\log L_{[\text{O II}]}$ at given M_{NUV} . It can be numerically calculated through

$$\log L_{[\text{O II}]}^{\text{exp}} = \xi_{\text{max}} = kM_{\text{NUV}} + b + \omega m_0(\alpha), \quad (6)$$

where $m_0(\alpha)$ is accurately approximated (Azzalini 2013) as

$$m_0(\alpha) = \mu_z - \frac{\gamma_1 \sigma_z}{2} - \frac{\text{sgn}(\alpha)}{2} e^{-\frac{2\pi}{|\alpha|}} \quad (7)$$

with

$$\begin{aligned} \delta &= \alpha / \sqrt{1 + \alpha^2}, \\ \mu_z &= \sqrt{2/\pi} \delta, \sigma_z = \sqrt{1 - \mu_z^2} \\ \gamma_1 &= \frac{4 - \pi}{2} \frac{(\delta \sqrt{2/\pi})^3}{(1 - 2\delta^2/\pi)^{3/2}} \end{aligned}$$

In principle, the intrinsic distribution $p^{\text{int}}(L_{[\text{O II}]}|M_{\text{NUV}})$ may be described by other suitable statistical models. The skew-normal distribution is just one concise model that is simple and can describe the intrinsic distribution well.

3.2. Method 1

In order to derive the intrinsic model for $p^{\text{int}}(L_{[\text{O II}]}|M_{\text{NUV}})$, we must properly take into account the incompleteness introduced by the $L_{[\text{O II}]}$ measurement. Namely, we should ensure that the $L_{[\text{O II}]}$ data is complete for a certain M_{NUV} . Nevertheless, for a part of [O II] emitters with weak emission lines or noisy spectra, it is difficult to derive their emission line profiles successfully, and thus these galaxies have low $SNRs$ of $L_{[\text{O II}]}$ measurement. Therefore, we regard a measurement of $SNR > 1$ as a meaningful one only.

For the purpose of overcoming this selection effect, in the first method (method 1) we attempt to construct a complete sample for $L_{[\text{O II}]}$ emitters. In analog to defining TSR and SSR , we define the measurement success rate (MSR) as the probability that the line flux is successfully measured for a galaxy of given M_{NUV} at redshift z . We divide the galaxies into two-dimensional

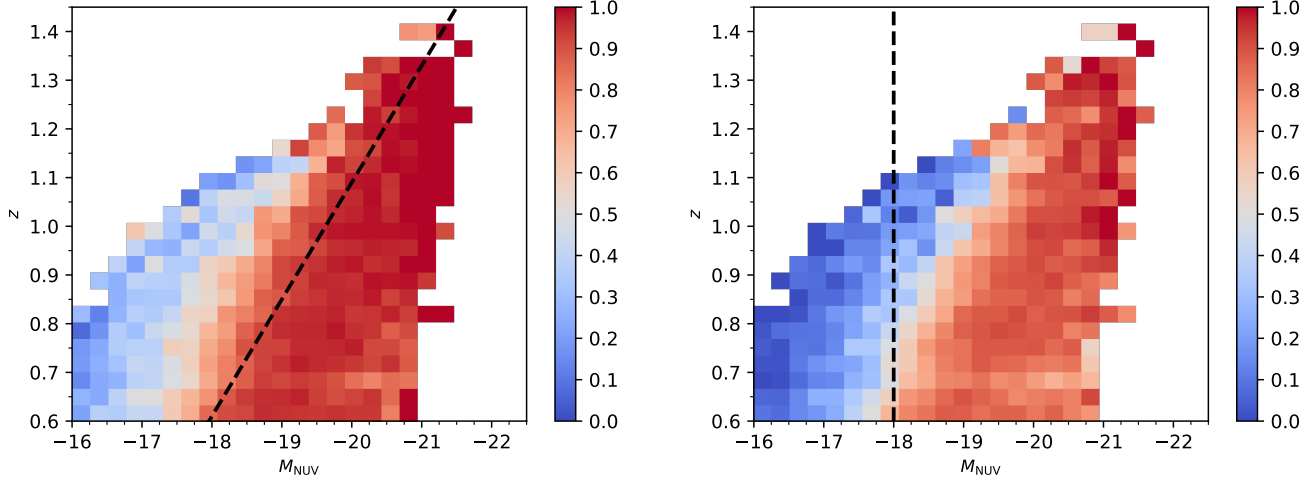


Figure 2. The measurement success rate (MSR) for [O II] emission lines. The left panel (for method 1) shows $MSR^{SNR>1} = N^w(SNR > 1)/N^w$, which is the ratio of the weighted number of galaxies with $L_{[\text{O II}]} SNR > 1$ to all galaxies in each M_{NUV} and redshift bin. Similar to the left panel, the right panel (for method 2) displays $MSR^{SNR>5} = N^w(SNR > 5)/N^w$. The color bar represents the value of the MSR at each bin. Both panels only show the bins each containing more than 20 galaxies. The two black dashed lines denote the M_{NUV} cut for the two methods. For method 1, we assume the galaxies falling into the region right of the black line have complete $L_{[\text{O II}]}$ measurement, and we use them for our modeling. Whereas, for method 2, we use all the galaxies in the region right of the black line ($M_{\text{NUV}} < -18$), regardless of their SNR , but we mask out those $L_{[\text{O II}]}$ with $SNR < 5$ in our fitting approach.

Table 1. The best-fitting model parameters with their 1σ uncertainties, and the number of galaxies used in the two methods.

Method	Redshift Range	N_{galaxy}	$N_{\text{galaxy}}^{SNR>1}$	$N_{\text{galaxy}}^{SNR>5}$	α	ω	k	b
Method 1	$0.6 \leq z < 0.7$...	10298	...	$-2.4719^{+0.0453}_{-0.0460}$	$0.3772^{+0.0026}_{-0.0026}$	-0.4	$34.0436^{+0.0024}_{-0.0024}$
	$0.7 \leq z < 0.8$...	8537	...	$-2.4270^{+0.0475}_{-0.0498}$	$0.3704^{+0.0028}_{-0.0028}$	-0.4	$34.0672^{+0.0027}_{-0.0027}$
	$0.8 \leq z < 0.9$...	5923	...	$-2.5072^{+0.0587}_{-0.0599}$	$0.3665^{+0.0032}_{-0.0032}$	-0.4	$34.0733^{+0.0030}_{-0.0030}$
	$0.9 \leq z < 1.0$...	4011	...	$-2.7083^{+0.0793}_{-0.0788}$	$0.3514^{+0.0036}_{-0.0036}$	-0.4	$34.0713^{+0.0033}_{-0.0034}$
	$1.0 \leq z < 1.1$...	1757	...	$-2.0849^{+0.0883}_{-0.0903}$	$0.3358^{+0.0052}_{-0.0054}$	-0.4	$34.1133^{+0.0054}_{-0.0056}$
	$0.6 \leq z < 1.45$...	31709	...	$-2.4357^{+0.0250}_{-0.0253}$	$0.3678^{+0.0014}_{-0.0014}$	-0.4	$34.0695^{+0.0013}_{-0.0013}$
Method 2	$0.6 \leq z < 0.7$	11799	...	9596	$-2.6805^{+0.0454}_{-0.0465}$	$0.4341^{+0.0031}_{-0.0030}$	-0.4	$34.0518^{+0.0025}_{-0.0025}$
	$0.7 \leq z < 0.8$	11062	...	9045	$-2.5538^{+0.0474}_{-0.0473}$	$0.4226^{+0.0031}_{-0.0032}$	-0.4	$34.0800^{+0.0026}_{-0.0027}$
	$0.8 \leq z < 0.9$	8679	...	6873	$-2.0802^{+0.0485}_{-0.0482}$	$0.4205^{+0.0040}_{-0.0040}$	-0.4	$34.0741^{+0.0037}_{-0.0037}$
	$0.9 \leq z < 1.0$	6113	...	4785	$-2.0293^{+0.0586}_{-0.0587}$	$0.3989^{+0.0046}_{-0.0046}$	-0.4	$34.0629^{+0.0042}_{-0.0044}$
	$1.0 \leq z < 1.1$	2791	...	2128	$-1.2168^{+0.0790}_{-0.0785}$	$0.3572^{+0.0078}_{-0.0078}$	-0.4	$34.0660^{+0.0098}_{-0.0104}$
	$0.6 \leq z < 1.45$	42392	...	34013	$-2.1387^{+0.0216}_{-0.0218}$	$0.4168^{+0.0017}_{-0.0017}$	-0.4	$34.0732^{+0.0015}_{-0.0015}$

bins according to their redshift and M_{NUV} , and then compute the $MSR^{SNR>1} = N^w(SNR > 1)/N^w$ as the ratio of the weighted number of galaxies with $SNR > 1$ to all galaxies in that bin. We display the $MSR^{SNR>1}$ as a function of M_{NUV} and redshift z in the left panel of Figure 2, where only the bins containing more than 20 galaxies are plotted. Apparently, at a given redshift, the MSR increases with the NUV brightness to a critical value M_{NUV}^c , and then stabilizes between 0.9 and

1 at $< M_{\text{NUV}}^c$. Furthermore, the MSR also decreases as the redshift increases at a given M_{NUV} . The black dashed line approximately represents the critical value M_{NUV}^c dividing the plot into two regions: in the right region (right of the dividing line) the $F_{[\text{O II}]}$ measurement is highly complete, with MSR being greater than 0.9 at almost all grid points and reaching 0.95 overall in the region. In the left region the measurement could be very incomplete, the effect of which must be taken

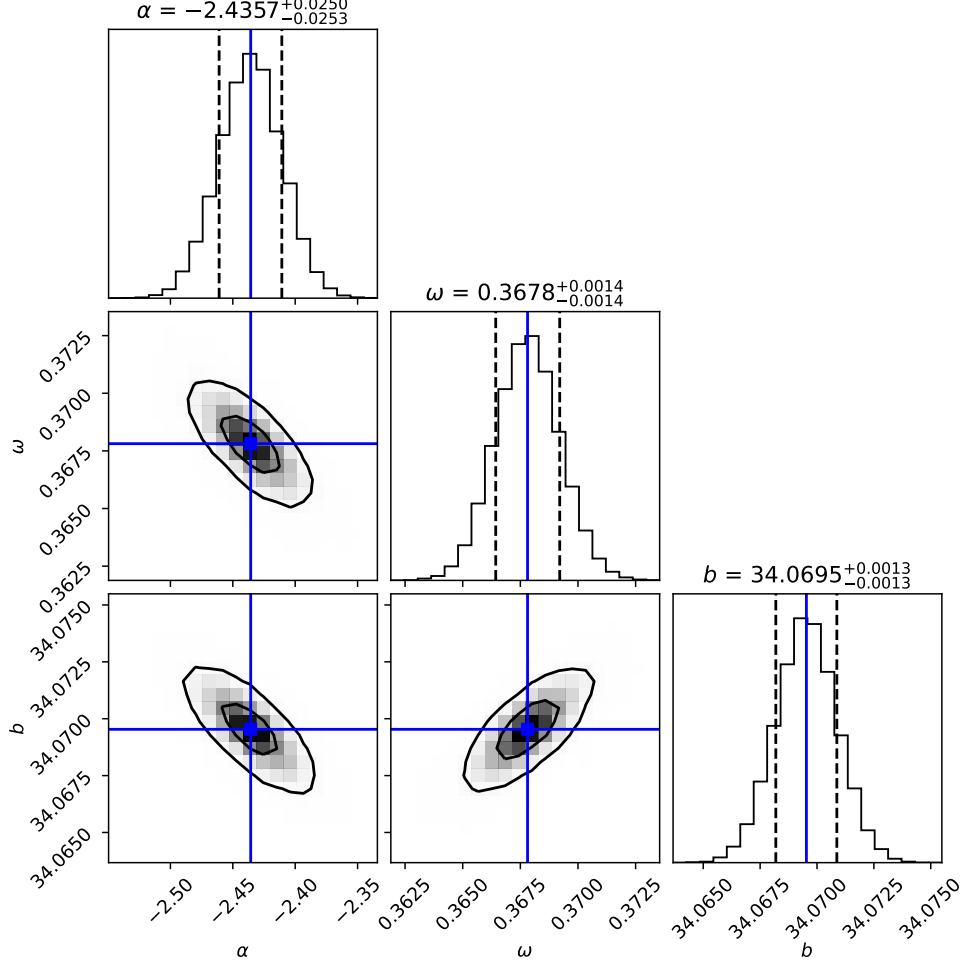


Figure 3. The joint posterior probability distribution for model parameters as well as their marginal probability distribution obtained by method 1 in the entire redshift range $0.6 \leq z < 1.45$. The best-fit values of α , ω and b are labeled as blue solid lines. The black dashed lines denote the 16% and 84% percentile of the marginal distribution. The confidence intervals of 68% (1σ) and 95% (2σ) are represented by the internal and external contours, respectively.

into account in the analysis. It should be noted that the measured $F_{[\text{O II}]}$ with low SNR may be fairly inaccurate even in the complete region. In other words, some galaxies with weak enough intrinsic [O II] luminosities may enter into the sample of $SNR > 1$ due to the photon noise in the measurements, and vice versa. To overcome the impurity and incompleteness effects, we must take the measurement uncertainties into consideration in our fitting process. As a result, for the i -th galaxy in our sample, we assume the observed $L_{[\text{O II}]}$ follow a Gaussian distribution for the given uncertainty $\sigma_{L_{[\text{O II}]}}^i$, and convolve this error distribution with the intrinsic PDF $p^{\text{int}}(L_{[\text{O II}]}|M_{\text{NUV}}^i)$ to account for the observed PDF

$$p^{\text{obs}}(L_{[\text{O II}]}| \theta, M_{\text{NUV}}^i, \sigma_{L_{[\text{O II}]}}^i) = \int p^{\text{int}}(L'_{[\text{O II}]}| \theta, M_{\text{NUV}}^i) \times N(L'_{[\text{O II}]} - L_{[\text{O II}]}^i | \sigma_{L_{[\text{O II}]}^i}) dL'_{[\text{O II}]}, \quad (8)$$

where the θ are the parameters of the intrinsic distribution (Equation 5). Consequently, the logarithmic likelihood function $\ln \mathcal{L}^{\text{M1}}$ for the first method M1 can be written as

$$\ln \mathcal{L}^{\text{M1}} = \sum_i w^i \ln p^{\text{obs}}(L_{[\text{O II}]}^i | \theta, M_{\text{NUV}}^i, \sigma_{L_{[\text{O II}]}^i}) \quad (9)$$

where the w^i is the weight of the i -th galaxy (Equation 1).

According to the Bayesian statistical theory, the posterior probability of the model parameters is proportional to the product of the likelihood function and the prior probability

$$p(\theta | L_{[\text{O II}]}, M_{\text{NUV}}, \sigma_{L_{[\text{O II}]}}) \propto \mathcal{L}(L_{[\text{O II}]} | \theta, M_{\text{NUV}}, \sigma_{L_{[\text{O II}]}}) \times p(\theta | M_{\text{NUV}}, \sigma_{L_{[\text{O II}]}}). \quad (10)$$

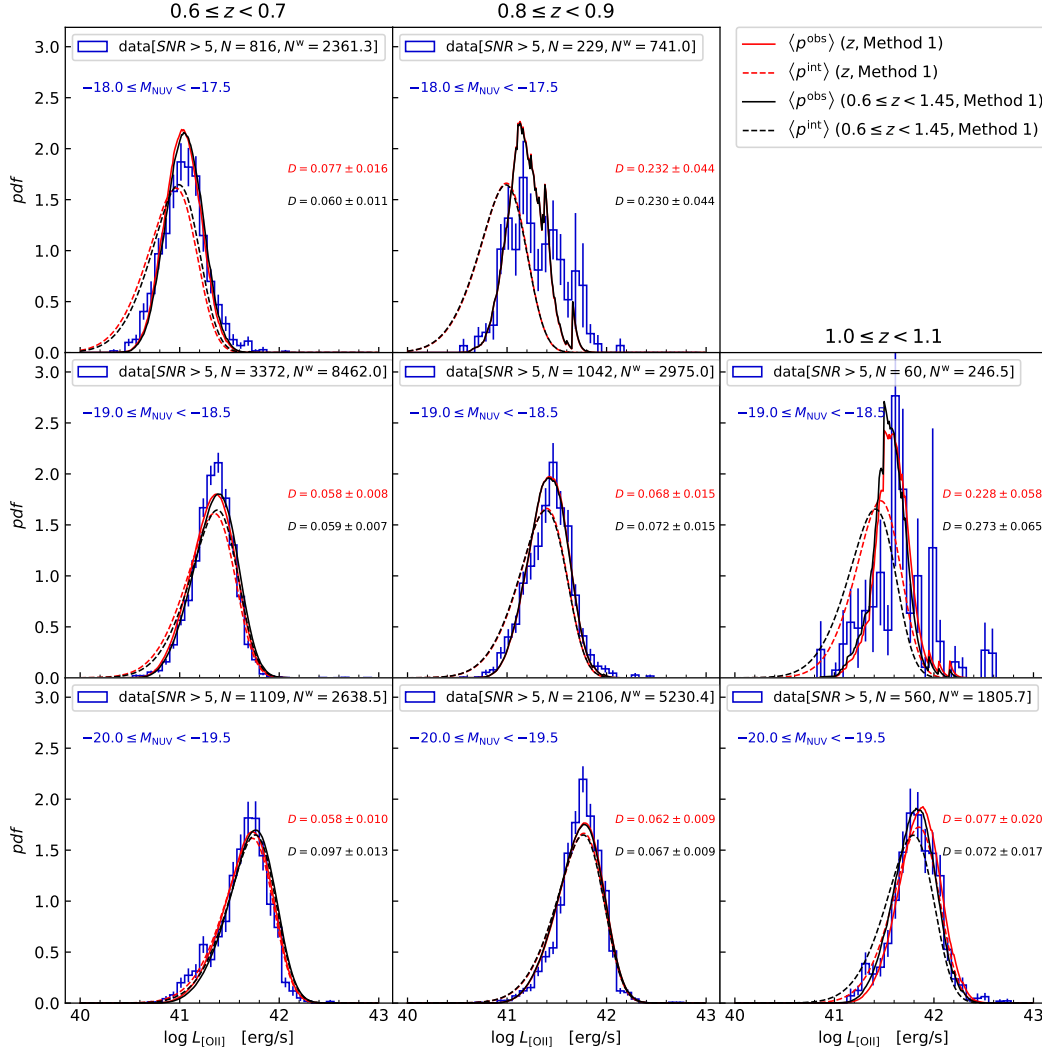


Figure 4. The observed $\log L_{[\text{O II}]}$ distribution of galaxies with $SNR > 5$ versus the model predictions with best-fit parameters derived by the method 1. The blue histograms with Poisson errors in each panel show the observed $\log L_{[\text{O II}]}$ distribution. Different panels in the same column show the distributions for different M_{NUV} at the same redshift. The solid lines represent our model $\langle p^{\text{obs}} \rangle$ calculated by Equation 11 for $SNR > 5$. For comparison, the average intrinsic distribution $\langle p^{\text{int}} \rangle$ defined by Equation 14 are plotted as dashed lines. We plot the model predictions with the best-fit parameters not only from the individual z bin itself but also from the entire redshift range $0.6 \leq z < 1.45$. Here the D , whose color corresponds to the color of the solid lines, is Kolmogorov-Smirnov (K-S) statistic that is used to quantify the maximum (supremum) distance between the CDF of the predicted distribution and the empirical cumulative distribution function (ECDF) of the ordered observational data.

Moreover, in order to investigate the redshift evolution of the intrinsic distribution, we divide the data into five redshift bins: $0.6 \leq z < 0.7$, $0.7 \leq z < 0.8$, $0.8 \leq z < 0.9$, $0.9 \leq z < 1.0$, $1.0 \leq z < 1.1$. The number of galaxies we used to fit in each redshift bin are shown in Table 1. Considering the proportional relationship between the luminosity of the NUV radiation and the luminosity of the [O II] emission line, we fix the slope k as -0.4 . In fact, we have tried to set k as a free parameter in the fitting, but we find that k is indeed close to -0.4 in all redshift bins. We choose the flat

prior distributions for the other three parameters: $-5 < \alpha < 5$, $0.1 < \omega < 1$, $0 < b < 50$.

We utilize the Markov Chain Monte Carlo (MCMC) approach to explore the space of the three parameters to obtain their posterior probability. A python package called as `emcee` (Foreman-Mackey et al. 2013) is used to perform the MCMC sampling in the parameter space. We randomly assign initial positions for 30 chains and run each chain by 5000 steps. The first 300 steps (about 10 times the integrated auto-correlation time) of each chain are discarded to ensure the convergence of the MCMC samples. In Table 1, we show the fitting re-

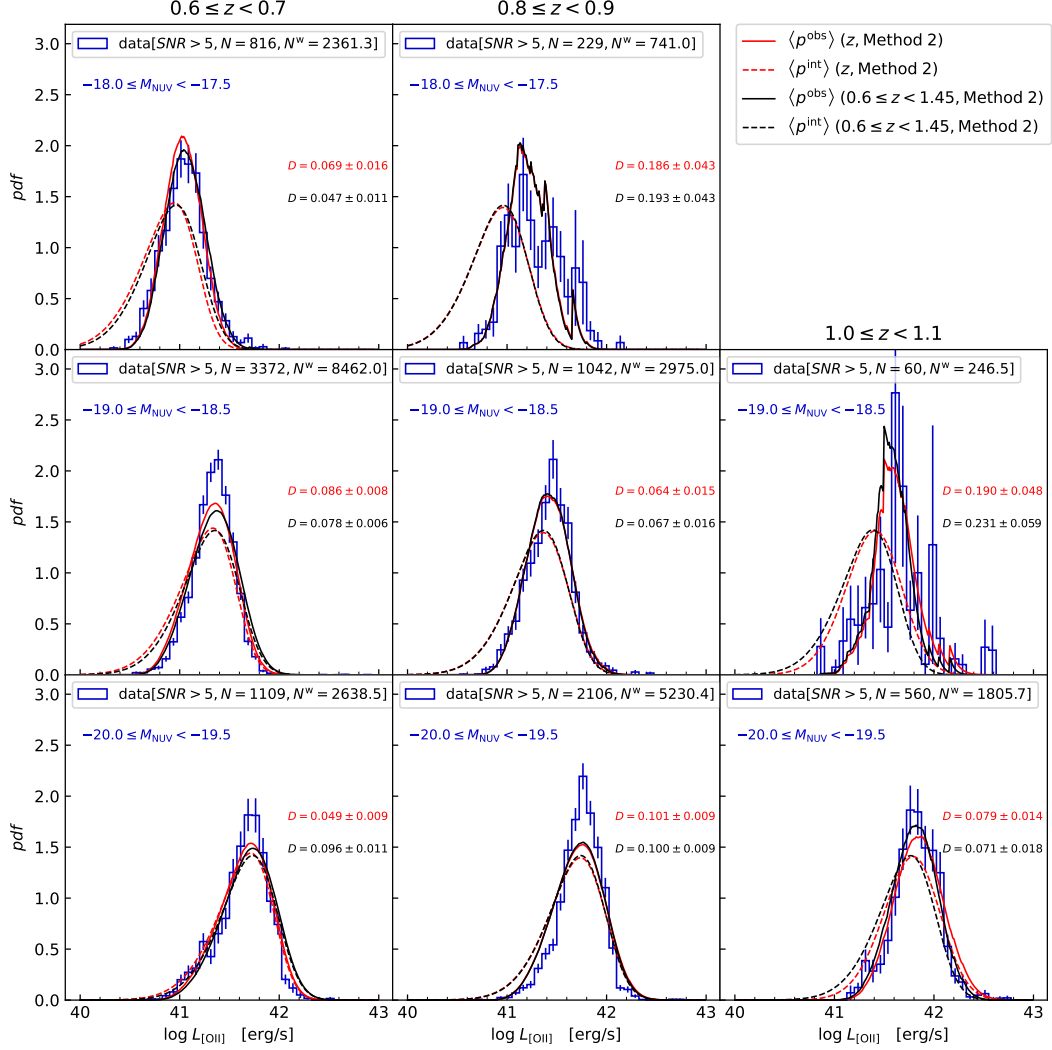


Figure 5. Same as Figure 4, but the $\langle p^{\text{obs}} \rangle$ and $\langle p^{\text{int}} \rangle$ are predicted with best-fit parameters derived by the method 2.

sults of these parameters as well as their 1σ error. We find that the parameters do not change significantly with the redshift in the range of $0.6 < z < 1.1$. This is very encouraging, as it implies that the parameters do not change either with the NUV luminosity because the sample contains more NUV luminous galaxies at a higher redshift. Therefore, we have also analyzed for the entire sample of galaxies within the redshift $0.6 \leq z < 1.45$, and list their model parameters in Table 1. We display the joint posterior probability distribution for any two of the parameters α , ω and b as well as the marginalized probability distribution for a single parameter in Figure 3 obtained by method 1 for the entire sample.

Let us first check the mean relationship of M_{NUV} and $L_{[\text{OII}]}$, which can be constructed with parameters k and b . For the purpose of exploring the redshift evolution of this relationship, using the Equation 6 and Equation 7, we numerically compute the $\log L_{[\text{OII}]}^{\text{exp}}$ of the $L_{[\text{OII}]}$

PDF at given M_{NUV} with the best-fit parameters in each redshift bin and show it in Figure 1 as a solid line. Meanwhile, the $\log L_{[\text{OII}]}^{\text{exp}}$ for the entire redshift range $0.6 \leq z < 1.45$ is also shown in the other panels as a dotted line. Although the best-fit b is slightly different at various redshifts, the $\log L_{[\text{OII}]}^{\text{exp}}$ does not indicate a significant redshift evolution trend. This fact suggests that the mean relationship of M_{NUV} and $L_{[\text{OII}]}$ is nearly redshift-independent and the assumption that $k = -0.4$ is reasonable.

Now let us further discuss about the distribution functions. In Figure 4, we display the observed PDF of $L_{[\text{OII}]}$ for galaxies with the $SNR > 5$ according to their M_{NUV} and z (histograms). We have used the weight w^i (Equation 1) to calculate the PDF and the Poisson error bars. In order to compare our best-fit intrinsic distribution function p^{int} with the observational histogram, we cal-

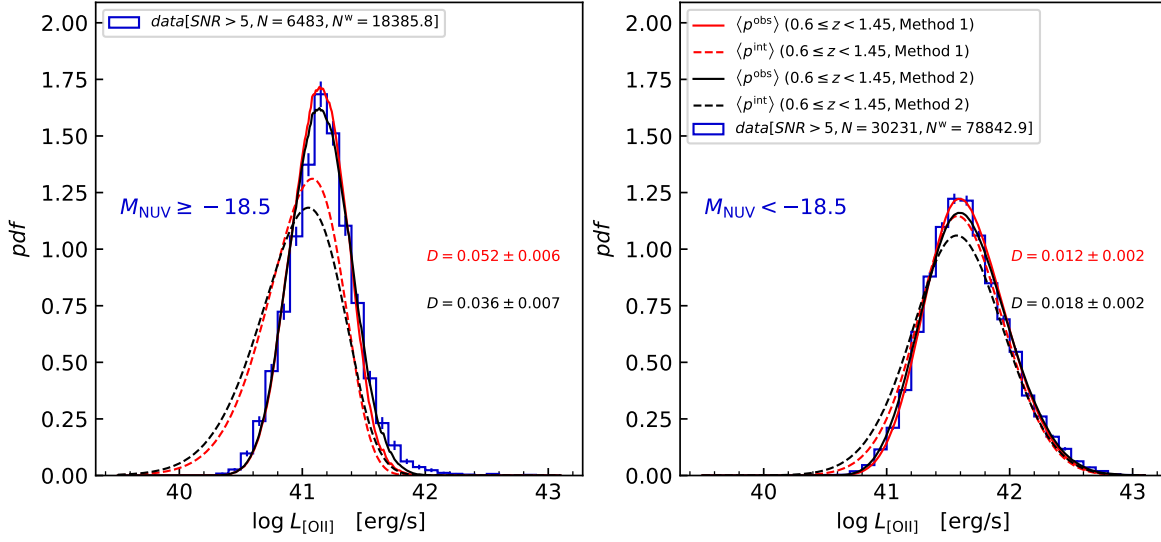
$0.6 \leq z < 1.45$


Figure 6. Same as Figure 4 and Figure 5, but we display the observed $L_{[\text{O II}]}$ distribution in the entire redshift range $0.6 \leq z < 1.45$. The left panel shows the distribution for the faint subsample ($M_{\text{NUV}} \geq -18.5$) and the right panel displays the one for the luminous subsample ($M_{\text{NUV}} < -18.5$). The $\langle p^{\text{obs}} \rangle$ and $\langle p^{\text{int}} \rangle$ are predicted with best-fit parameters derived by the both methods.

culate the weighted average observed PDF $\langle p^{\text{obs}} \rangle$ by

$$\langle p^{\text{obs}} \rangle = \frac{\sum_i w^i p^{\text{obs}, \text{cod}}(L_{[\text{O II}]} | M_{\text{NUV}}^i, \sigma_{L_{[\text{O II}]}^i})}{\sum_i w^i}, \quad (11)$$

where the $p^{\text{obs}, \text{cod}}$ expressed as

$$\begin{aligned} & p^{\text{obs}, \text{cod}}(L_{[\text{O II}]} | M_{\text{NUV}}^i, \sigma_{L_{[\text{O II}]}^i}) \\ &= \frac{p^{\text{obs}}(L_{[\text{O II}]} | M_{\text{NUV}}^i, \sigma_{L_{[\text{O II}]}^i})}{1 - C^{\text{obs}}(L_{[\text{O II}], \text{thr}}^i | M_{\text{NUV}}^i, \sigma_{L_{[\text{O II}]}^i})} \end{aligned} \quad (12)$$

is the conditional PDF for the cut of $SNR > 5$ and C^{obs} expressed as

$$\begin{aligned} & C^{\text{obs}}(L_{[\text{O II}], \text{thr}}^i | \theta, M_{\text{NUV}}^i, \sigma_{L_{[\text{O II}]}^i}) \\ &= \int^{L_{[\text{O II}], \text{thr}}^i} p^{\text{obs}}(L'_{[\text{O II}]} | \theta, M_{\text{NUV}}^i, \sigma_{L_{[\text{O II}]}^i}) dL'_{[\text{O II}]} \end{aligned} \quad (13)$$

represents the cumulative probability function (CDF) of the observational distribution p^{obs} below the [O II] SNR threshold ($L_{[\text{O II}], \text{thr}}^i = 5\sigma_{L_{[\text{O II}]}^i}$ for the i -th galaxy).

Obviously, with $\langle p^{\text{obs}} \rangle$ we have properly accounted for the incompleteness of measuring the [O II] line flux for given redshift and M_{NUV} . The fitted curves $\langle p^{\text{obs}} \rangle$ based on the method 1 overall match well with the observed ones. The parameters we obtained for the entire sample

of $0.6 \leq z < 1.45$ also fit with the subsample at different redshift. To make a statistical comparison, we tried to assess this method and (or) possible redshift dependence of the parameters by taking the non-parametric Kolmogorov-Smirnov (K-S) test (Kolmogorov-Smirnov et al. 1933; Smirnov 1948). We calculate the empirical cumulative distribution function (ECDF) of the ordered observational data, and compare it to the CDF of the distribution $\langle p^{\text{obs}} \rangle$. The maximum (supremum) distance between the ECDF and CDF is defined as the K-S statistic D . To evaluate the impact of sample size, we estimate the 1σ uncertainty of D by the bootstrap re-sampling method and annotate their values in each panel of Figure 4. For one observed distribution (one panel of Figure 4), the statistic D for a single redshift $\langle p^{\text{obs}} \rangle(z)$ is close to that for the entire redshift range $\langle p^{\text{obs}} \rangle(0.6 \leq z < 1.45)$, thus we do not find any significant redshift dependence of the parameters.

It would be interesting to compare the intrinsic distribution p^{int} with the $\langle p^{\text{obs}} \rangle$. Considering the range of M_{NUV} of the galaxies at each redshift bin, we calculate the average intrinsic PDF $\langle p^{\text{int}} \rangle$ by

$$\langle p^{\text{int}} \rangle = \frac{\sum_i w^i p^{\text{int}}(L_{[\text{O II}]} | M_{\text{NUV}}^i)}{\sum_i w^i}, \quad (14)$$

and we have plotted them as the dashed lines in Figure 4. The figure shows that the faint subsample ($M_{\text{NUV}} \geq -18.5$) are very incomplete at all redshift, and the brighter ones become increasingly incomplete with

redshift. This indicates how important it is to correct for the incompleteness in deriving the intrinsic distributions. Clearly, for both the $\langle p^{\text{int}} \rangle$ and $\langle p^{\text{obs}} \rangle$, the PDF for the entire redshift range $0.6 \leq z < 1.45$ is close to that for each single redshift bin. It means that not only the mean relationship of M_{NUV} and $L_{[\text{O II}]}$ but also the intrinsic scatter distribution of $L_{[\text{O II}]}$ at given M_{NUV} is nearly redshift independent.

3.3. Method 2

In our method 1, although we have ensured the completeness of [O II] flux measurement at $\sim 95\%$ level and have also corrected for the influence of measurement errors, we have had to adopt the critical value M_{NUV}^c that limits the number of galaxies we can use. In order to check whether our results are robust to the selection of the complete sample, we develop the second method (method 2) to account for the incompleteness in a different way. We also use the *MSR*, but here we calculate $MSR^{SNR>5} = N^w(SNR > 5)/N^w$ that is the probability of measuring $L_{[\text{O II}]}$ with high $SNR > 5$, and display it in the right panel of Figure 2. We assume that those [O II] lines with $SNR > 5$ can be 100% successfully measured. In the opposite, for the remaining galaxies with $SNR < 5$, we regard their $L_{[\text{O II}]}$ as unsuccessfully measured. However, we notice that $MSR^{SNR>5}$ becomes very low for those faint galaxies ($M_{\text{NUV}} > -18$), which may make our fitting results unstable. For instance, the $MSR^{SNR>5}$ at $M_{\text{NUV}} = -16$ is less than 0.3 at any redshift, namely, at least 70% galaxies have not been measured in their $L_{[\text{O II}]}$ fluxes. For this reason, in our fitting process, we make a loose M_{NUV} cut criteria ($M_{\text{NUV}} < -18$) and plotted it as the black dashed line in the right panel of Figure 2, which enables us to avoid censoring too much data. It should be emphasized that we use *all* the galaxies in the region right to this dividing line, i.e. we have not only included the galaxies whose [O II] fluxes have been measured successfully ($SNR > 5$), but also the ones with SNR below the threshold $SNR = 5$ or even with negative $SNR < 0$. In statistics, the concept of this kind of model regression problem in which the data is censored (true value is unknown but the dividing threshold is known) is firstly proposed by Tobin (1958). Hartley & Swanson (1985) summarize this regression problem and show its application in the maximum likelihood estimation (MLE). Referring to this MLE method, we construct the logarithmic

likelihood function $\ln \mathcal{L}^{\text{M2}}$ for the second method

$$\begin{aligned} \ln \mathcal{L}^{\text{M2}} &= \sum_i \left[(1 - f^i) w^i \ln C^{\text{obs}} \left(L_{[\text{O II}],\text{thr}}^i | \theta, M_{\text{NUV}}^i, \sigma_{L_{[\text{O II}]}}^i \right) \right. \\ &\quad \left. + f^i w^i \ln p^{\text{obs}} \left(L_{[\text{O II}]}^i | \theta, M_{\text{NUV}}^i, \sigma_{L_{[\text{O II}]}}^i \right) \right], \end{aligned} \quad (15)$$

where f^i is a step function indicating whether its $L_{[\text{O II}]}$ measurement is successful,

$$f^i(SNR) = \begin{cases} 0, & \text{if } SNR < 5 \\ 1, & \text{if } SNR \geq 5 \end{cases}, \quad (16)$$

w^i is the weighting factor and C^{obs} defined by Equation 13 represents the CDF at 5σ threshold ($L_{[\text{O II}],\text{thr}}^i = 5\sigma_{L_{[\text{O II}]}}^i$).

We use the same MCMC fitting scheme as described in Section 3.2 for method 2 and show the best-fit parameters in Table 1. Analogous to method 1, the $\log L_{[\text{O II}]}^{\text{exp}}$ derived from method 2 is plotted as the black line in Figure 1. The comparisons between the observational distributions and the model predictions $\langle p \rangle$ for method 2 are displayed in Figure 5.

From Figure 1, comparing the results from method 1 and method 2, we find the corresponding $\log L_{[\text{O II}]}^{\text{exp}}$ are very close to each other in the low redshift range $0.6 \leq z < 0.8$ where the measurement of $L_{[\text{O II}]}$ is relatively complete. For the higher redshift range $0.8 \leq z < 1.1$, $\log L_{[\text{O II}]}^{\text{exp}}$ of method 2 shows a lower intercept, maybe due to the fact that method 2 uses more galaxies that have $SNR < 1$ which were otherwise excluded in method 1 and makes the $\log L_{[\text{O II}]}^{\text{exp}}$ shift to a lower luminosity. Additionally, the $L_{[\text{O II}]}^{\text{exp}}$ of method 2 appears to be more stable at different z , even for the highest redshift range $1.0 \leq z < 1.1$ where the $\log L_{[\text{O II}]}^{\text{exp}}$ still agrees very well with the one derived from the entire sample ($0.6 \leq z < 1.45$). It may indicate that the method 2 can better correct for the bias caused by the incomplete measurements and recover the intrinsic $\log L_{[\text{O II}]}^{\text{exp}}$. But in any case, the difference between the intercepts obtained from the two methods and (or) for the different redshift bins is always less than 0.1 dex (see also Table 1), indicating that the mean relation between the luminosity of $L_{[\text{O II}]}$ and NUV is both nearly redshift independent.

We further compare the distribution functions obtained by the two methods in Figure 6, where we show the observed $L_{[\text{O II}]}$ distribution and predicted $\langle p \rangle$ in the entire redshift range $0.6 \leq z < 1.45$. On one hand, compared to the method 1, the intrinsic distribution $\langle p^{\text{int}} \rangle$ for method 2 tends to be more extended towards the low $L_{[\text{O II}]}$ end. This is exactly what we expected, since we

use more galaxies with weak or undetected [O II] emission line in method 2. Besides, although the best-fit parameters α and ω for the two methods have obvious divergence, their observed distributions $\langle p^{\text{obs}} \rangle$ are relatively consistent in general. This characteristic can be interpreted as the degeneracy of α and ω , the absolute value of α increases with ω but the shape of the skew-normal distribution does not change much. On the other hand, the $\langle p^{\text{obs}} \rangle$ from the method 1 seems to be closer to the observation than that from method 2 in the luminous bin ($M_{\text{NUV}} < -18.5$), but in the faint bin ($M_{\text{NUV}} \geq -18.5$) where the $L_{[\text{O II}]}$ measurement is more incomplete, the method 2 shows better results because it utilizes extra information from the $L_{[\text{O II}]}$ measurements with $SNR < 1$ compared to method 1. In general, both methods can yield a universal distribution function that can reproduce the observed $L_{[\text{O II}]}$ distributions regardless of their redshift. Therefore, combining the NUV LF at a certain redshift, we can use the intrinsic conditional distribution functions $p^{\text{int}}(L_{[\text{O II}]}^i | M_{\text{NUV}}^i)$ to predict the [O II] LF at that redshift.

Furthermore, recently Favole et al. (2020) adopts three different semi-analytical models (SAMs) running on the MultiDark2 simulation (Klypin et al. 2016) to study the properties of mocked [O II] emitters. They have established the linear scaling relations between $L_{[\text{O II}]}$ and the observed-frame absolute magnitude M_u and M_g at $z = 0.94$, where the observed u and g magnitudes are good proxies of the rest-frame M_{NUV} luminosity. They show that the [O II] LF can be reproduced well using the $\log L_{[\text{O II}]} - M_u(M_g)$ relation especially for the SAGE model (Croton et al. 2016). It is worth mentioning that the slope $-0.373(-0.342)$ and intercept $34.01(34.29)$ of the linear relationship $\log L_{[\text{O II}]} - M_u(M_g)$ derived from the SAGE model are quite close to our observational results. Therefore, our observed $L_{[\text{O II}]} - M_{\text{NUV}}$ relation can be used to calibrate the SAM of galaxy formation.

In APPENDIX B, we check the effect of SNR threshold and cosmic variance on the $p^{\text{int}}(L_{[\text{O II}]} | M_{\text{NUV}})$. As shown in Figure 13, the intrinsic $L_{[\text{O II}]}$ conditional distributions derived from different SNR thresholds or different sky fields all present similar skewed shapes. In addition, although we have selected a complete sample and corrected the measurement effects as much as possible, the conditional distribution function $p^{\text{int}}(L_{[\text{O II}]} | M_{\text{NUV}})$ at very faint M_{NUV} cannot be well constrained if those galaxies are undetected. The future PFS survey with high quality spectra will provide opportunities to further test our result on faint galaxies.

4. PREDICTION FOR THE LUMINOSITY FUNCTION AND COUNT OF THE [O II] EMITTERS

4.1. Prediction of the [O II] luminosity function

Convolving the intrinsic PDF $p^{\text{int}}(L_{[\text{O II}]} | M_{\text{NUV}})$ with NUV luminosity function $\Phi(M_{\text{NUV}})$, we can proceed to predict the [O II] LF by

$$\Phi(L_{[\text{O II}]}) = \int p^{\text{int}}(L_{[\text{O II}]} | M_{\text{NUV}}) \Phi(M_{\text{NUV}}) dM_{\text{NUV}}. \quad (17)$$

Here, we adopt three $\Phi(M_{\text{NUV}})$ from the literature. For the high redshift range ($z > 0.6$), we choose the NUV LF recently measured by Moutard et al. (2020) based on two state-of-the-art photometric survey Canada-France-Hawaii Telescope Large Area U-band Deep Survey (CLAUDS, Sawicki et al. 2019) and HyperSuprime-Cam Subaru Strategic Program (HSC-SSP, Aihara et al. 2018) as well as the UV photometry from the GALEX satellite (Martin et al. 2005). Although Moutard et al. (2020) has measured $\Phi(M_{\text{NUV}})$ at eight redshift bins from $z = 0.05$ to $z = 3.5$ and provides their best-fit parameters of the classical Schechter function (Schechter 1976), the relatively small sky area (18.29 deg^2) and the uncertainty of photometric redshift may affect the NUV LF measurement especially in the low redshift range (because the photo- z uncertainty is proportional to $1 + z$). Therefore, we also adopt other NUV LFs measured with precise spectroscopic redshift data in the lower redshift bins. One is that measured by Robotham & Driver (2011) at the local universe $0 < z < 0.1$ using the data from SDSS DR7 (Abazajian et al. 2009) and GALEX MIS (Morrissey et al. 2007). Another is that given by Cucciati et al. (2012) based on VVDS survey (Le Fèvre et al. 2005, 2013), for which we use the best-fit Schechter parameters in redshift bin $0.2 < z < 0.4$ and $0.4 < z < 0.6$.

The red and black solid lines in Figure 7 are our predicted [O II] LFs from method 1 and method 2 respectively. By comparison, the method 2 predicts more luminous [O II] emitters, albeit the difference is very small. For the purpose of comparing our prediction with the observation, the [O II] LFs calculated with the best-fit Schechter (Schechter 1976) parameters obtained by recent observational studies (Ciardullo et al. 2013; Comparat et al. 2015; Sobral et al. 2015; Khostovan et al. 2015; Hayashi et al. 2018) are presented in Figure 7. In particular, Comparat et al. (2016) and Saito et al. (2020) have modeled the [O II] LF as a function of redshift, thus enabling us to calculate the [O II] LF at the mean redshift in each interval. As displayed in Figure 7, for the lowest redshift bin $0 < z < 0.1$, the predicted [O II]

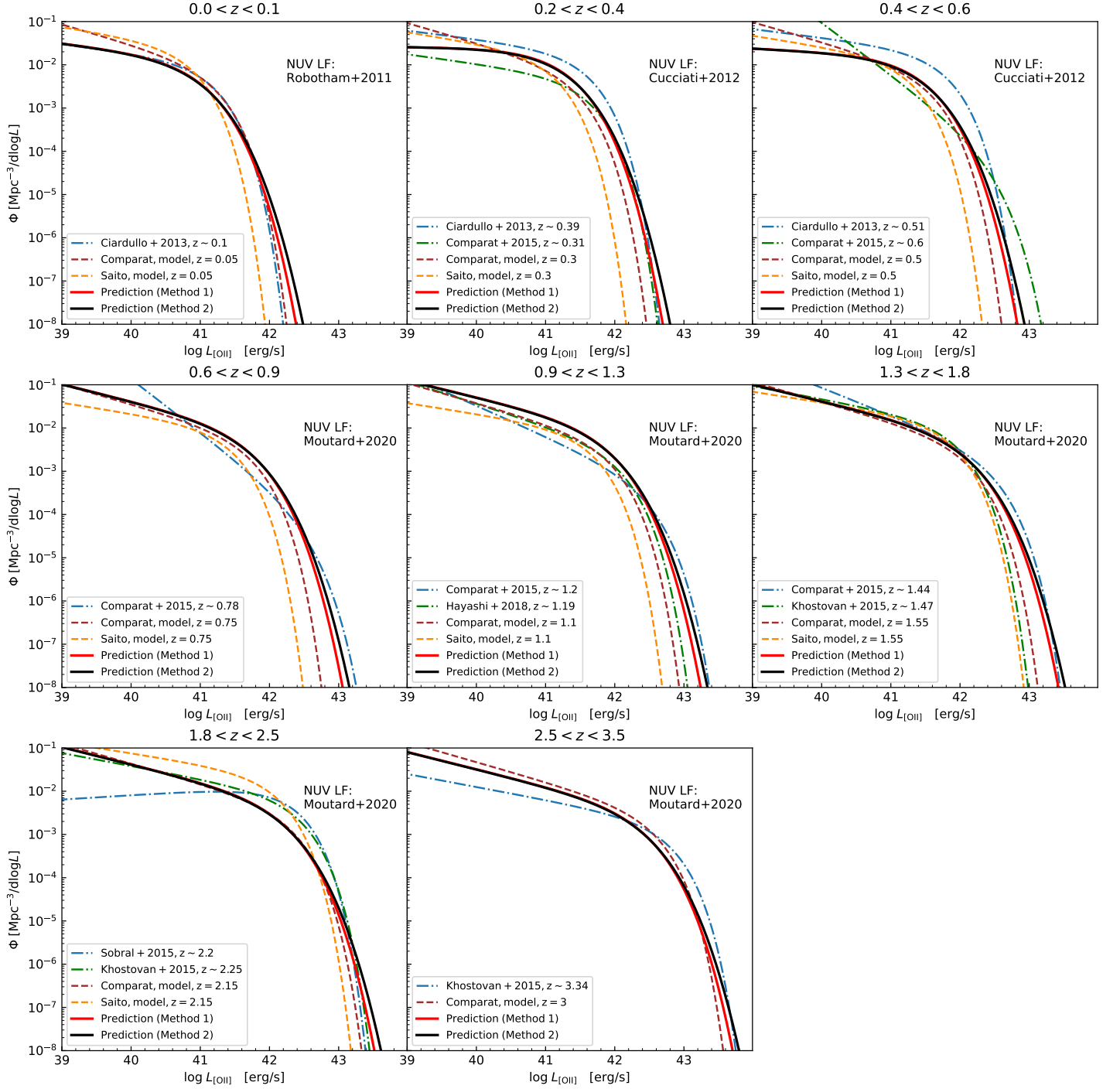


Figure 7. The comparison of our predicted [O II] luminosity function (LF) with the observational results from the literature at different redshift. The red and black solid lines show our predicted [O II] LFs, derived by convolving the NUV LFs measured by Robotham & Driver (2011), Cucciati et al. (2012) and Moutard et al. (2020) in different redshift intervals with our best-fit model $p^{\text{int}}(L_{[\text{O II}]}/M_{\text{NUV}})$ obtained by method 1 and method 2, respectively. The dash-dotted lines with different colors represent the observed LFs calculated with the the best-fit Schechter (Schechter 1976) parameters in some recent measurements (Ciardullo et al. 2013; Comparat et al. 2015; Sobral et al. 2015; Khostovan et al. 2015; Hayashi et al. 2018). Additionally, using two redshift dependent Schechter LF models proposed by Comparat et al. (2016) and Saito et al. (2020), we calculate [O II] LFs at the mean redshift of each z interval, and plot them as brown and orange dashed lines in each panel respectively.

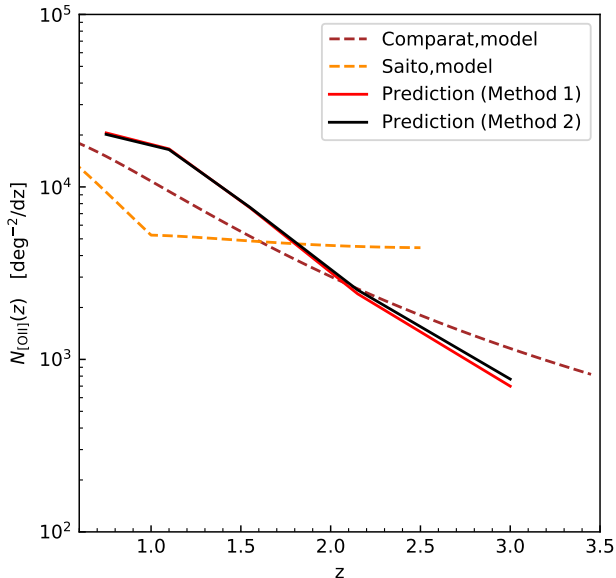


Figure 8. The prediction for the number counts of galaxies with [O II] flux greater than $6.3 \times 10^{-17} \text{ergs}^{-1} \text{cm}^{-2}$. Two solid lines correspond to our predictions based on our two methods, which nearly overlap each other. The brown and orange dashed lines represent the $N_{[\text{O II}]}$ calculated based on the [O II] LF models developed by Comparat et al. (2016) and Saito et al. (2020) respectively. The model of Saito et al. (2020) was calibrated up to redshift 2.5 only by the authors.

LF tends to slightly over-predict the number density of very luminous [O II] emitters, while for the redshift intervals $0.6 < z < 0.9$ and $0.9 < z < 1.3$ our prediction shows a slightly higher number density of galaxies for $\log L_{[\text{O II}]} < 42$. Nevertheless, given the large uncertainties and (or) variations of the current observed [O II] LFs, our predictions overall agree rather well with the observations in the entire redshift range $z < 3.5$. Specifically, even for the highest redshift bin $2.5 < z < 3.5$, the predicted [O II] LF is still close to the observation, which further supports that the intrinsic distribution of $L_{[\text{O II}]}$ at given M_{NUV} is likely to be universal.

4.2. Prediction of [O II] number counts

Furthermore, using our predicted [O II] LFs at $z < 3.5$, we calculate the number counts per deg^2 per redshift for [O II] emitters. We adopt the same flux limit $F_{\text{lim}} = 6.3 \times 10^{-17} \text{ergs}^{-1} \text{cm}^{-2}$ as Saito et al. (2020), where the F_{lim} is about six times the averaged noise expected for the PFS survey. Our two methods turn out nearly identical predictions. For comparison, we also compute the $N_{[\text{O II}]}(z)$ based on two empirical [O II] LF models proposed by Comparat et al. (2016) and Saito et al. (2020). As displayed in Figure 8, our predicted $N_{[\text{O II}]}-z$ is quite close to the model of Comparat et al. (2016), though our prediction has a slightly steeper slope. In the redshift

range $0.6 < z < 1.6$, our model predicts more [O II] emitters, while our model prediction drops more rapidly than the other two models for $z > 2$. Especially for redshift $z = 2.5$ which is of high interest to the PFS survey, our prediction is a factor 5 lower than the model of Saito et al. (2020), and is about 30% lower than the model of Comparat et al. (2016).

5. SUMMARY

In this study, we construct the intrinsic connection between the [O II] emission line luminosity $L_{[\text{O II}]}$ and the rest-frame near-ultraviolet band absolute magnitude M_{NUV} based on a large sample of galaxies from the VIPERS survey. We summarize our main results as follows:

1. By analyzing the calibrated spectra, we have measured the [O II] flux for 54166 galaxies in the redshift range of $0.6 \leq z < 1.45$. Combining the eight-band photometric data, we also perform the SED template fitting to obtain the rest-frame NUV absolute magnitude M_{NUV} for each galaxy.
2. We propose an intrinsic conditional PDF model $p^{\text{int}}(L_{[\text{O II}]}|M_{\text{NUV}})$ to describe the probability distribution of $L_{[\text{O II}]}$ at a given M_{NUV} . This model is constructed by a linear relationship of $\log L_{[\text{O II}]} - M_{\text{NUV}}$ with a skew-lognormal distribution of $L_{[\text{O II}]}$, and can be characterized by three parameters. We develop two different methods to carefully correct for the incompleteness and measurement uncertainty of $L_{[\text{O II}]}$. Having accounted for these observational effects in our likelihood analysis, we derive the best-fit intrinsic model parameters through an MCMC approach.
3. Comparing the best-fit model with the observed data at different z , we find that the mean linear relationship $\log L_{[\text{O II}]} - M_{\text{NUV}}$ is almost redshift independent. The constant slope $k = -0.4$ indicates that the luminosity of [O II] is proportional to that of NUV. To further investigate the probability distribution of $L_{[\text{O II}]}$ at given M_{NUV} , we divide galaxies into various M_{NUV} and redshift bins, and compare the observed distribution of $L_{[\text{O II}]}$ with our predicted $p^{\text{obs}}(L_{[\text{O II}]}|M_{\text{NUV}})$ from the best-fit model. The comparison demonstrates that the both methods can yield the universal conditional PDF of $L_{[\text{O II}]}$, which depends on neither NUV luminosity nor redshift. This $L_{[\text{O II}]} - M_{\text{NUV}}$ relation can complement the recent research of Favole et al. (2020) based on simulation, and provides a feasible approach to calibrate the SAM models.

4. Convoluting the $L_{[\text{O II}]}$ conditional PDF with the NUV LFs adopted from the literature, we have predicted the [O II] LFs at eight redshift bins spanning from $z = 0$ to 3.5. Our predicted [O II] LFs are broadly consistent with the observational results from previous studies, though the published $L_{[\text{O II}]}$ LFs often have significant variations. It further supports that the conditional PDF of $L_{[\text{O II}]}$ is universal. We also have estimated the number counts $N_{[\text{O II}]}(z)$ of [O II] emitters for the forthcoming PFS survey at the flux detection limit of $6.3 \times 10^{-17} \text{ergs}^{-1} \text{cm}^{-2}$. The predicted $N_{[\text{O II}]}(z)$ is close to that calculated by the model of [Comparat et al. \(2016\)](#). At $z = 2.5$ which is of high interest to the PFS survey, our predicted number count is 5 times lower than the model of [Saito et al. \(2020\)](#).

In conclusion, the universal conditional PDF of $L_{[\text{O II}]}$ can be used to efficiently pre-select candidates for bright [O II] emitters, and it thus will play a significant role in optimizing the source selection strategy for future galaxy redshift surveys. Moreover, this universal $L_{[\text{O II}]} - M_{\text{NUV}}$ distribution function directly constructs the intrinsic relationship between the ultraviolet radiation and the [O II] line emission for star-forming galaxies. It will also help us to understand the formation mechanism of the [O II] emission in galaxies.

ACKNOWLEDGMENTS

H.Y.G is truly grateful to Huanian Zhang for his kind help in measuring the flux of [O II] emission lines. H.Y.G also thanks Jiaxin Han for useful discussions about Bayesian analysis. The work is supported by NSFC (11533006, 11621303, 11890691) and by 111 project No. B20019. We gratefully acknowledge the support of the Key Laboratory for Particle Physics, Astrophysics and Cosmology, Ministry of Education.

This paper uses data from the VIMOS Public Extragalactic Redshift Survey (VIPERS). VIPERS has been performed using the ESO Very Large Telescope, under the "Large Programme" 182.A-0886. The participating institutions and funding agencies are listed at <http://vipers.inaf.it>. Based on observations collected at the European Southern Observatory, Cerro Paranal, Chile, using the Very Large Telescope under programs 182.A-0886 and partly 070.A-9007. Also based on observations obtained with MegaPrime/MegaCam, a joint project of CFHT and CEA/DAPNIA, at the Canada-France-Hawaii Telescope (CFHT), which is operated by the National Research Council (NRC) of Canada, the Institut National des Sciences de l'Univers of the Cen-

tre National de la Recherche Scientifique (CNRS) of France, and the University of Hawaii. This work is based in part on data products produced at TERAPIX and the Canadian Astronomy Data Centre as part of the CanadaFrance-Hawaii Telescope Legacy Survey, a collaborative project of NRC and CNRS. This research uses data from the VIMOS VLT Deep Survey, obtained from the VVDS database operated by Cesam, Laboratoire d'Astrophysique de Marseille, France.

Software: Numpy ([van der Walt et al. 2011](#)), Scipy ([Oliphant 2007](#)), Matplotlib ([Hunter 2007](#)), Astropy ([Astropy Collaboration et al. 2013](#)), emcee ([Foreman-Mackey et al. 2013](#))

APPENDIX

A. THE CHECKING OF [O II] FLUX AND STATISTICS OF THE GALAXY SAMPLES

[Lamareille et al. \(2009\)](#) have released their measured [O II] flux in the VVDS-22h wide field (F22) of the VIMOS VLT Deep Survey (VVDS, [Le Fèvre et al. 2005, 2013](#)), which enables us to check our method for the [O II] measurement. We apply our method to the same galaxies in the VVDS-22h wide field (F22) to measure their [O II] flux. A comparison between the two measurements is presented in [Figure 9](#), which shows a very good agreement. We note a small systematic difference (less than 10%) at small flux which may be attributed to the difference of the two studies in subtracting the continuum, as [Lamareille et al. \(2009\)](#) used a combination of stellar population templates to model the stellar component of the spectra but we use a sixth-order polynomial to describe the continuum around the [O II] line.

We apply this method to the VIPERS galaxies with redshift flag ≥ 2 in the range of $0.6 \leq z < 1.45$. For those weak or noisy spectral lines, the fitting may fail, and/or the covariance matrix of the parameters may not be calculated correctly. Here, we define a line fitting as being successful if following three conditions are satisfied: (a) $F_{[\text{O II}]} > 0$, (b) the diagonal elements of the covariance matrix are positive, and (c) the uncertainty of line width $\sigma_{W_{[\text{O II}]}} < 100 \text{\AA}$ (the fitted line widths $W_{[\text{O II}]}$ are normally between 3-10 \AA , so we remove those with $\sigma_{W_{[\text{O II}]}} \geq 100 \text{\AA}$ that are obviously outliers). As the result, 45139 out of the total 54166 galaxies have been successfully fitted.

Nonetheless, it should be emphasized that in our method 2 (see [Equation 13](#) and [15](#)), we use all galaxies, not only those fitted successfully ($SNR > 0$), to ensure that our sample is complete. Therefore, for

the purpose of determining the SNR threshold (e.g. $L_{[\text{O II}],\text{thr}}^i = 5\sigma_{L_{[\text{O II}]}}^i$), we also need to estimate the measurement uncertainty for the lines that failed to be fitted. In order to estimate their $\sigma_{F_{[\text{O II}]}}$, we calculate the ratio of $\sigma_{F_{[\text{O II}]}}^i$ to $\langle\sigma^i\rangle$ for each galaxies with $SNR > 0$, here the $\sigma_{F_{[\text{O II}]}}^i$ is derived from the covariance matrix and the $\langle\sigma^i\rangle$ is the average of noise spectrum in the fitting range ($3727 \pm 20\text{\AA}$) for the i -th galaxy. As displayed in the left panel of Figure 10, $\sigma_{F_{[\text{O II}]}}^i$ is roughly proportional to $\langle\sigma^i\rangle$ for the galaxies with high SNR . The mean ratio $\langle\sigma_{F_{[\text{O II}]}}^i / \langle\sigma^i\rangle\rangle (SNR > 5) = 11.653\text{\AA}$ is plotted as a solid brown line in Figure 10. Hence it enables us to approximately estimate the $\sigma_{F_{[\text{O II}]}}^i$ through multiplying this mean ratio by the average background noise ($\sigma_{F_{[\text{O II}]}}^i \simeq 11.653\text{\AA} \times \langle\sigma^i\rangle$) for those galaxies that failed being fitted. As a note, one may also estimate the $\sigma_{F_{[\text{O II}]}}^i$ from the error propagation of noise spectrum (the root-sum-square of noise spectrum in the range of $3727 \pm 20\text{\AA}$ times the spacing of pixels $\Delta\lambda$), and we show it in the right panel of Figure 10. The two estimates are similar for the [O II] with high SNR , but the errors from the covariance matrix are more dispersive at low SNR , reflecting the additional errors associated with the measurement of the [O II] line. We used these two types of errors in our statistical study of the relation between [O II] and NUV luminosities, and found that the result is insensitive to which type of error used. In this paper, we adopt the $\sigma_{F_{[\text{O II}]}}^i$ estimated from the covariance matrix.

Finally, in Figure 11, we present the distributions of [O II] luminosity, SNR , uncertainty and redshift of galaxies in our sample.

B. TEST THE EFFECT OF SIGNAL-TO-NOISE RATIO AND COSMIC VARIANCE ON THE SKEWED SHAPE OF $L_{[\text{O II}]}$ CONDITIONAL DISTRIBUTION

In this appendix, we investigate two factors that may impact the intrinsic shape of the $L_{[\text{O II}]}$ conditional probability distribution function (PDF for short). One is the specific values (1 and 5) set for the SNR threshold in method 1 and method 2 respectively (see also Section 3). We should carefully analyze the influence of this factor on the shape of the PDF at the faint end. Considering that some spurious [O II] emitters with $SNR < 5$ could affect the purity of our samples, we adopt $SNR = 3$ as a new threshold in method 2. The MSR of our samples is shown in Figure 12.

The other factor is the effect of a finite survey volume or sample size, usually called as the cosmic variance. The cosmic variance could more likely affect the shape

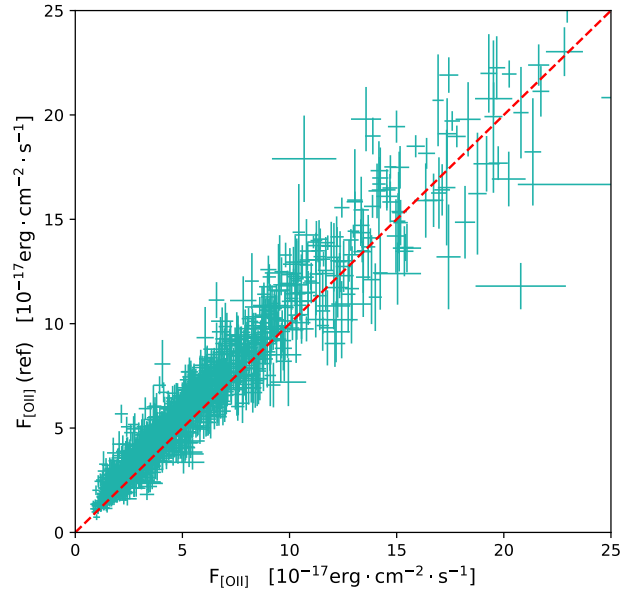


Figure 9. A check of our [O II] flux measurement method. The $F_{[\text{O II}]}$ is the [O II] flux measured with our method for galaxies in the VVDS-22h wide field (F22) of the VIMOS VLT Deep Survey (VVDS, Le Fèvre et al. 2005, 2013), compared with the $F_{[\text{O II}]}(\text{ref})$ of the previous measurement from Lamareille et al. (2009). The measurements with $SNR > 5$ are displayed together as green points with horizontal and vertical error bars. The red dashed line represents that $F_{[\text{O II}]}(\text{ref}) = F_{[\text{O II}]}$.

of [O II] PDF at the bright end where the number of luminous galaxies is small. Therefore, we divide our galaxy sample into three fields: W1(RA ≤ 34.5 deg), W1(RA > 34.5 deg) and W4, and repeat the method 2 to derive the intrinsic [O II] PDF in each field. The results are displayed in in Table 2.

We plot the three intrinsic PDF $p^{\text{int}}(L_{[\text{O II}]}|M_{\text{NUV}})$ calculated at $M_{\text{NUV}} = -20$ in Figure 13. By comparison, the intrinsic [O II] PDF in all three fields exhibit similar skew-normal ($\alpha < 0$) shape, while the expectation value $\log L_{[\text{O II}]}^{\text{exp}}$ in W4 is about 0.05 dex (see also Table 2) brighter than that in W1. This means that cosmic variance hardly affects the shape of the [O II] PDF, but has a slight effect on the intercept of the $\log L_{[\text{O II}]} - M_{\text{NUV}}$ relation. On the other hand, to explore the influence of the SNR threshold, we also plot the intrinsic [O II] PDF derived from the threshold of $SNR = 5$ (the last row of Table 1) as a red line in Figure 13. Although the PDF derived from $SNR > 5$ is slightly more concentrated than that derived from $SNR > 3$, they both show a skew-normal shape extending to the faint side.

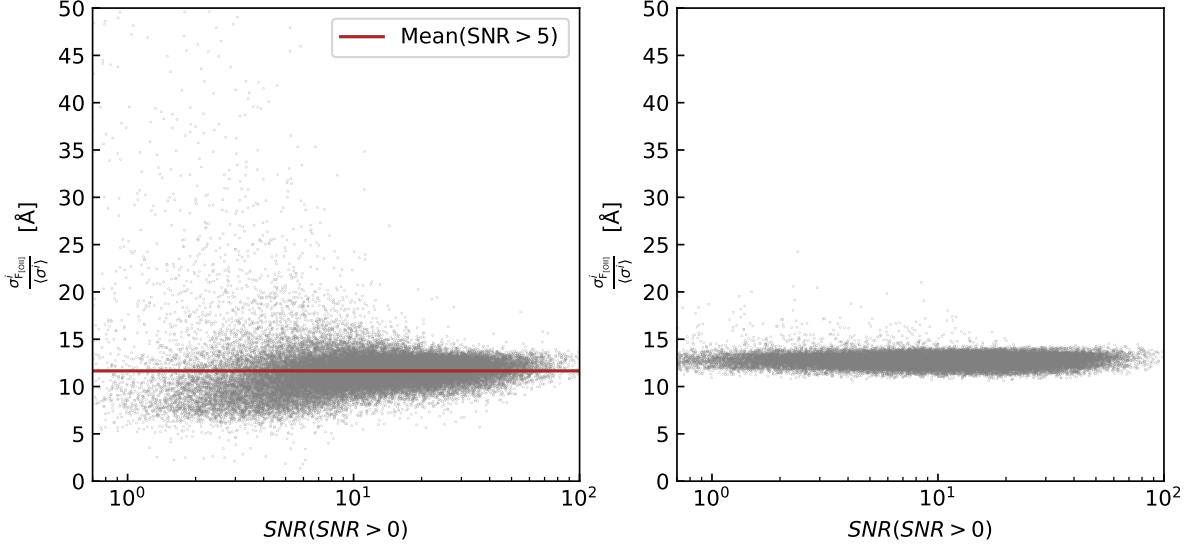


Figure 10. The ratio of the flux uncertainty $\sigma_{F_{[\text{O II}]}}^i$ to the average background noise $\langle \sigma^i \rangle$ in the range of $3727 \pm 20 \text{ \AA}$ as a function of SNR . Each gray point corresponds to a galaxy in our VIPERS sample. The $\sigma_{F_{[\text{O II}]}}^i$ in the left panel and right panel is estimated from the covariance matrix and the error propagation of noise spectrum, respectively. The solid brown line in the left panel shows the mean ratio $\langle \sigma_{F_{[\text{O II}]}}^i / \langle \sigma^i \rangle \rangle = 11.653 \text{ \AA}$ for the galaxies with $SNR > 5$.

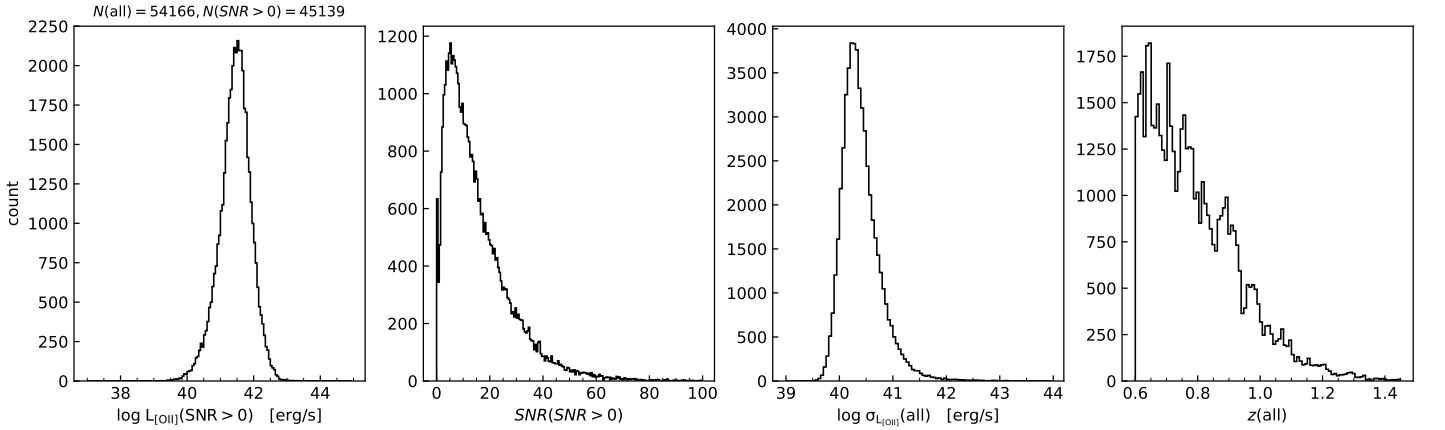


Figure 11. The distributions of [O II] luminosity $L_{[\text{O II}]}$, SNR , uncertainty $\sigma_{L_{[\text{O II}]}}$ and redshift of our galaxy sample.

We have also checked the sensitivity of our result to the SNR threshold in method 1. We repeated the cal-

culatation by setting $SNR > 0$, and found the result has little changed.

Therefore, our results are robust both to the reasonable values set for the SNR thresholds and to the cosmic variance as the sample is sufficiently large.

REFERENCES

- Abazajian, K. N., Adelman-McCarthy, J. K., Agüeros, M. A., et al. 2009, *ApJS*, 182, 543, doi: [10.1088/0067-0049/182/2/543](https://doi.org/10.1088/0067-0049/182/2/543)
- Aihara, H., Arimoto, N., Armstrong, R., et al. 2018, *PASJ*, 70, S4, doi: [10.1093/pasj/psx066](https://doi.org/10.1093/pasj/psx066)
- Argence, B., & Lamareille, F. 2009, *A&A*, 495, 759, doi: [10.1051/0004-6361/20066998](https://doi.org/10.1051/0004-6361/20066998)
- Arnouts, S., Moscardini, L., Vanzella, E., et al. 2002, *MNRAS*, 329, 355, doi: [10.1046/j.1365-8711.2002.04988.x](https://doi.org/10.1046/j.1365-8711.2002.04988.x)

Table 2. Similar to Table 1. The best-fitting model parameters with their 1σ uncertainties are derived from galaxies with SNR threshold equal to 3 in three survey fields.

Method	Redshift Range	Field	N_{galaxy}	$N_{\text{galaxy}}^{SNR>3}$	α	ω	k	b
Method 2	$0.6 \leq z < 1.45$	W1(RA \leq 34.5 deg)	14723	12927	$-2.4109^{+0.0363}_{-0.0363}$	$0.4419^{+0.0028}_{-0.0027}$	-0.4	$34.0711^{+0.0023}_{-0.0024}$
	$0.6 \leq z < 1.45$	W1(RA $>$ 34.5 deg)	14099	12418	$-2.3235^{+0.0361}_{-0.0367}$	$0.4463^{+0.0029}_{-0.0028}$	-0.4	$34.0797^{+0.0026}_{-0.0025}$
	$0.6 \leq z < 1.45$	W4	13570	11691	$-2.5648^{+0.0379}_{-0.0385}$	$0.4590^{+0.0029}_{-0.0029}$	-0.4	$34.1263^{+0.0023}_{-0.0024}$

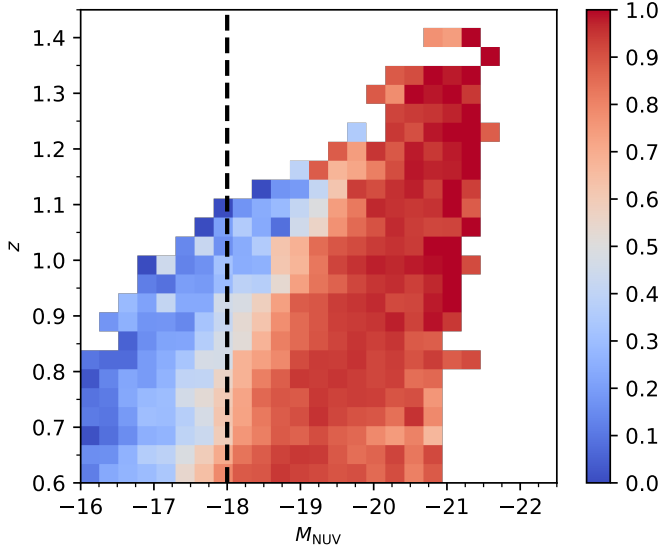


Figure 12. Similar to Figure 2, the panel shows $MSR^{SNR>3} = N^w(SNR > 3)/N^w$.

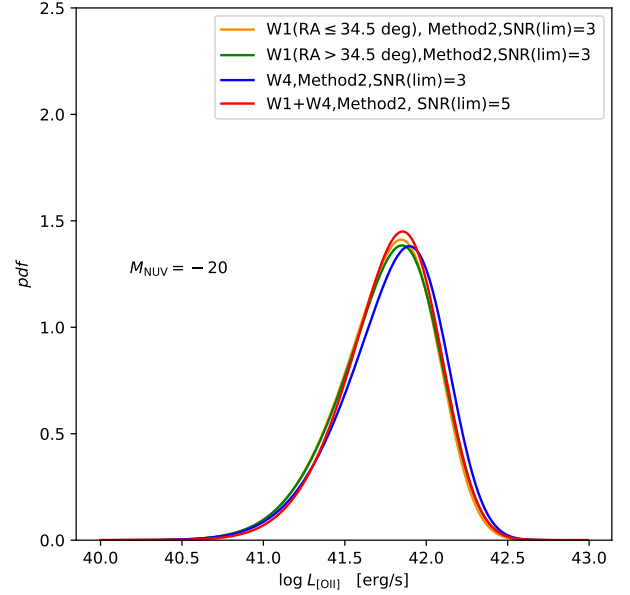


Figure 13. The intrinsic PDF $p^{\text{int}}(L_{[\text{O III}]}|M_{\text{NUV}})$ calculated with the best-fitting parameters at $M_{\text{NUV}} = -20$. The orange, green and blue lines corresponding to the three rows of Table 2 represent the PDF derived at $SNR > 3$ in three different fields. For comparison, the PDF derived at $SNR > 5$ using all galaxies (the last row of Table 1) is plotted as a red line.

Astropy Collaboration, Robitaille, T. P., Tollerud, E. J., et al. 2013, *A&A*, 558, A33, doi: [10.1051/0004-6361/201322068](https://doi.org/10.1051/0004-6361/201322068)

Atek, H., Malkan, M., McCarthy, P., et al. 2010, *ApJ*, 723, 104, doi: [10.1088/0004-637X/723/1/104](https://doi.org/10.1088/0004-637X/723/1/104)

Atek, H., Siana, B., Scarlata, C., et al. 2011, *ApJ*, 743, 121, doi: [10.1088/0004-637X/743/2/121](https://doi.org/10.1088/0004-637X/743/2/121)

Azzalini, A. 2013, *The skew-normal and related families*, Vol. 3 (Cambridge University Press)

Bayliss, K. D., McMahon, R. G., Venemans, B. P., Ryan-Weber, E. V., & Lewis, J. R. 2011, *MNRAS*, 413, 2883, doi: [10.1111/j.1365-2966.2011.18360.x](https://doi.org/10.1111/j.1365-2966.2011.18360.x)

Bruzual, G., & Charlot, S. 2003, *MNRAS*, 344, 1000, doi: [10.1046/j.1365-8711.2003.06897.x](https://doi.org/10.1046/j.1365-8711.2003.06897.x)

Calzetti, D., Armus, L., Bohlin, R. C., et al. 2000, *ApJ*, 533, 682, doi: [10.1086/308692](https://doi.org/10.1086/308692)

Chabrier, G. 2003, *PASP*, 115, 763, doi: [10.1086/376392](https://doi.org/10.1086/376392)

Ciardullo, R., Gronwall, C., Adams, J. J., et al. 2013, *ApJ*, 769, 83, doi: [10.1088/0004-637X/769/1/83](https://doi.org/10.1088/0004-637X/769/1/83)

Cole, S., Percival, W. J., Peacock, J. A., et al. 2005, *MNRAS*, 362, 505, doi: [10.1111/j.1365-2966.2005.09318.x](https://doi.org/10.1111/j.1365-2966.2005.09318.x)

Comparat, J., Richard, J., Kneib, J.-P., et al. 2015, *A&A*, 575, A40, doi: [10.1051/0004-6361/201424767](https://doi.org/10.1051/0004-6361/201424767)

Comparat, J., Zhu, G., Gonzalez-Perez, V., et al. 2016, *MNRAS*, 461, 1076, doi: [10.1093/mnras/stw1393](https://doi.org/10.1093/mnras/stw1393)

Croton, D. J., Stevens, A. R. H., Tonini, C., et al. 2016, *ApJS*, 222, 22, doi: [10.3847/0067-0049/222/2/22](https://doi.org/10.3847/0067-0049/222/2/22)

Cucciati, O., Tresse, L., Ilbert, O., et al. 2012, *A&A*, 539, A31, doi: [10.1051/0004-6361/201118010](https://doi.org/10.1051/0004-6361/201118010)

De Barros, S., Oesch, P. A., Labbé, I., et al. 2019, *MNRAS*, 489, 2355, doi: [10.1093/mnras/stz940](https://doi.org/10.1093/mnras/stz940)

de Jong, R. S., Agertz, O., Berbel, A. A., et al. 2019, *The Messenger*, 175, 3, doi: [10.18727/0722-6691/5117](https://doi.org/10.18727/0722-6691/5117)

DESI Collaboration, Aghamousa, A., Aguilar, J., et al. 2016, arXiv e-prints, arXiv:1611.00036. <https://arxiv.org/abs/1611.00036>

- Draine, B. T. 2011, *Physics of the Interstellar and Intergalactic Medium*
- Drake, A. B., Simpson, C., Collins, C. A., et al. 2013, *MNRAS*, 433, 796, doi: [10.1093/mnras/stt775](https://doi.org/10.1093/mnras/stt775)
- Eisenstein, D. J., Zehavi, I., Hogg, D. W., et al. 2005, *ApJ*, 633, 560, doi: [10.1086/466512](https://doi.org/10.1086/466512)
- Favole, G., Gonzalez-Perez, V., Stoppacher, D., et al. 2020, *MNRAS*, 497, 5432, doi: [10.1093/mnras/staa2292](https://doi.org/10.1093/mnras/staa2292)
- Foreman-Mackey, D., Hogg, D. W., Lang, D., & Goodman, J. 2013, *PASP*, 125, 306, doi: [10.1086/670067](https://doi.org/10.1086/670067)
- Gallego, J., García-Dabó, C. E., Zamorano, J., Aragón-Salamanca, A., & Rego, M. 2002, *ApJL*, 570, L1, doi: [10.1086/340830](https://doi.org/10.1086/340830)
- Garilli, B., Guzzo, L., Scodreggio, M., et al. 2014, *A&A*, 562, A23, doi: [10.1051/0004-6361/201322790](https://doi.org/10.1051/0004-6361/201322790)
- Gilbank, D. G., Baldry, I. K., Balogh, M. L., Glazebrook, K., & Bower, R. G. 2010, *MNRAS*, 405, 2594, doi: [10.1111/j.1365-2966.2010.16640.x](https://doi.org/10.1111/j.1365-2966.2010.16640.x)
- Green, J., Schechter, P., Baltay, C., et al. 2012, arXiv e-prints, arXiv:1208.4012. <https://arxiv.org/abs/1208.4012>
- Guzzo, L., Scodreggio, M., Garilli, B., et al. 2014, *A&A*, 566, A108, doi: [10.1051/0004-6361/201321489](https://doi.org/10.1051/0004-6361/201321489)
- Hartley, M. J., & Swanson, E. V. 1985, Maximum likelihood estimation of the truncated and censored normal regression models (The World Bank)
- Hayashi, M., Tanaka, M., Shimakawa, R., et al. 2018, *PASJ*, 70, S17, doi: [10.1093/pasj/psx088](https://doi.org/10.1093/pasj/psx088)
- Hippelein, H., Maier, C., Meisenheimer, K., et al. 2003, *A&A*, 402, 65, doi: [10.1051/0004-6361:20021898](https://doi.org/10.1051/0004-6361:20021898)
- Hunter, J. D. 2007, *Computing in Science Engineering*, 9, 90
- Ilbert, O., Arnouts, S., McCracken, H. J., et al. 2006, *A&A*, 457, 841, doi: [10.1051/0004-6361:20065138](https://doi.org/10.1051/0004-6361:20065138)
- Jarvis, M. J., Bonfield, D. G., Bruce, V. A., et al. 2013, *MNRAS*, 428, 1281, doi: [10.1093/mnras/sts118](https://doi.org/10.1093/mnras/sts118)
- Kaiser, N. 1987, *MNRAS*, 227, 1, doi: [10.1093/mnras/227.1.1](https://doi.org/10.1093/mnras/227.1.1)
- Kennicutt, Robert C., J. 1998, *ARA&A*, 36, 189, doi: [10.1146/annurev.astro.36.1.189](https://doi.org/10.1146/annurev.astro.36.1.189)
- Kewley, L. J., Geller, M. J., & Jansen, R. A. 2004, *AJ*, 127, 2002, doi: [10.1086/382723](https://doi.org/10.1086/382723)
- Khostovan, A. A., Sobral, D., Mobasher, B., et al. 2015, *MNRAS*, 452, 3948, doi: [10.1093/mnras/stv1474](https://doi.org/10.1093/mnras/stv1474)
- Klypin, A., Yepes, G., Gottlöber, S., Prada, F., & Heß, S. 2016, *Monthly Notices of the Royal Astronomical Society*, 457, 4340, doi: [10.1093/mnras/stw248](https://doi.org/10.1093/mnras/stw248)
- Kolmogorov-Smirnov, A., Kolmogorov, A., & Kolmogorov, M. 1933
- Lamareille, F., Brinchmann, J., Contini, T., et al. 2009, *A&A*, 495, 53, doi: [10.1051/0004-6361:200810397](https://doi.org/10.1051/0004-6361:200810397)
- Laureijs, R., Amiaux, J., Arduini, S., et al. 2011, arXiv e-prints, arXiv:1110.3193. <https://arxiv.org/abs/1110.3193>
- Le Fèvre, O., Saisse, M., Mancini, D., et al. 2003, *Society of Photo-Optical Instrumentation Engineers (SPIE) Conference Series*, Vol. 4841, Commissioning and performances of the VLT-VIMOS instrument, ed. M. Iye & A. F. M. Moorwood, 1670–1681, doi: [10.1117/12.460959](https://doi.org/10.1117/12.460959)
- Le Fèvre, O., Vettolani, G., Garilli, B., et al. 2005, *A&A*, 439, 845, doi: [10.1051/0004-6361:20041960](https://doi.org/10.1051/0004-6361:20041960)
- Le Fèvre, O., Cassata, P., Cucciati, O., et al. 2013, *A&A*, 559, A14, doi: [10.1051/0004-6361/201322179](https://doi.org/10.1051/0004-6361/201322179)
- Levenberg, K. 1944, *Quarterly of applied mathematics*, 2, 164
- Ly, C., Malkan, M. A., Kashikawa, N., et al. 2007, *ApJ*, 657, 738, doi: [10.1086/510828](https://doi.org/10.1086/510828)
- Marquardt, D. W. 1963, *Journal of the society for Industrial and Applied Mathematics*, 11, 431
- Martin, D. C., Fanson, J., Schiminovich, D., et al. 2005, *ApJL*, 619, L1, doi: [10.1086/426387](https://doi.org/10.1086/426387)
- Mehta, V., Scarlata, C., Colbert, J. W., et al. 2015, *ApJ*, 811, 141, doi: [10.1088/0004-637X/811/2/141](https://doi.org/10.1088/0004-637X/811/2/141)
- Merson, A., Wang, Y., Benson, A., et al. 2018, *MNRAS*, 474, 177, doi: [10.1093/mnras/stx2649](https://doi.org/10.1093/mnras/stx2649)
- Morrissey, P., Conrow, T., Barlow, T. A., et al. 2007, *ApJS*, 173, 682, doi: [10.1086/520512](https://doi.org/10.1086/520512)
- Moustakas, J., & Kennicutt, Robert C., J. 2006, *ApJS*, 164, 81, doi: [10.1086/500971](https://doi.org/10.1086/500971)
- Moutard, T., Sawicki, M., Arnouts, S., et al. 2020, *MNRAS*, doi: [10.1093/mnras/staa706](https://doi.org/10.1093/mnras/staa706)
- Moutard, T., Arnouts, S., Ilbert, O., et al. 2016, *A&A*, 590, A102, doi: [10.1051/0004-6361/201527945](https://doi.org/10.1051/0004-6361/201527945)
- Oesterbrock, D. 1974
- O'hagan, A., & Leonard, T. 1976, *Biometrika*, 63, 201
- Oliphant, T. E. 2007, *Computing in Science Engineering*, 9, 10
- Park, K., Di Matteo, T., Ho, S., et al. 2015, *MNRAS*, 454, 269, doi: [10.1093/mnras/stv1954](https://doi.org/10.1093/mnras/stv1954)
- Pozzetti, L., Hirata, C. M., Geach, J. E., et al. 2016, *A&A*, 590, A3, doi: [10.1051/0004-6361/201527081](https://doi.org/10.1051/0004-6361/201527081)
- Rigopoulou, D., Vacca, W. D., Berta, S., Franceschini, A., & Aussel, H. 2005, *A&A*, 440, 61, doi: [10.1051/0004-6361:20034109](https://doi.org/10.1051/0004-6361:20034109)
- Robotham, A. S. G., & Driver, S. P. 2011, *MNRAS*, 413, 2570, doi: [10.1111/j.1365-2966.2011.18327.x](https://doi.org/10.1111/j.1365-2966.2011.18327.x)
- Saito, S., de la Torre, S., Ilbert, O., et al. 2020, *MNRAS*, 494, 199, doi: [10.1093/mnras/staa727](https://doi.org/10.1093/mnras/staa727)

- Sawicki, M., Arnouts, S., Huang, J., et al. 2019, MNRAS, 489, 5202, doi: [10.1093/mnras/stz2522](https://doi.org/10.1093/mnras/stz2522)
- Schechter, P. 1976, ApJ, 203, 297, doi: [10.1086/154079](https://doi.org/10.1086/154079)
- Schlegel, D. J., Finkbeiner, D. P., & Davis, M. 1998, ApJ, 500, 525, doi: [10.1086/305772](https://doi.org/10.1086/305772)
- Scodreggio, M., Guzzo, L., Garilli, B., et al. 2018, A&A, 609, A84, doi: [10.1051/0004-6361/201630114](https://doi.org/10.1051/0004-6361/201630114)
- Smirnov, N. 1948, The annals of mathematical statistics, 19, 279
- Sobral, D., Best, P. N., Matsuda, Y., et al. 2012, MNRAS, 420, 1926, doi: [10.1111/j.1365-2966.2011.19977.x](https://doi.org/10.1111/j.1365-2966.2011.19977.x)
- Sobral, D., Smail, I., Best, P. N., et al. 2013, MNRAS, 428, 1128, doi: [10.1093/mnras/sts096](https://doi.org/10.1093/mnras/sts096)
- Sobral, D., Matthee, J., Best, P. N., et al. 2015, MNRAS, 451, 2303, doi: [10.1093/mnras/stv1076](https://doi.org/10.1093/mnras/stv1076)
- Spergel, D., Gehrels, N., Baltay, C., et al. 2015, arXiv e-prints, arXiv:1503.03757.
<https://arxiv.org/abs/1503.03757>
- Takada, M., Ellis, R. S., Chiba, M., et al. 2014, PASJ, 66, R1, doi: [10.1093/pasj/pst019](https://doi.org/10.1093/pasj/pst019)
- Takahashi, M. I., Shioya, Y., Taniguchi, Y., et al. 2007, ApJS, 172, 456, doi: [10.1086/518037](https://doi.org/10.1086/518037)
- Teplitz, H. I., Collins, N. R., Gardner, J. P., Hill, R. S., & Rhodes, J. 2003, ApJ, 589, 704, doi: [10.1086/374659](https://doi.org/10.1086/374659)
- Tobin, J. 1958, Econometrica: journal of the Econometric Society, 24
- Valentino, F., Daddi, E., Silverman, J. D., et al. 2017, MNRAS, 472, 4878, doi: [10.1093/mnras/stx2305](https://doi.org/10.1093/mnras/stx2305)
- van der Walt, S., Colbert, S. C., & Varoquaux, G. 2011, Computing in Science Engineering, 13, 22
- Zhai, Z., Benson, A., Wang, Y., Yepes, G., & Chuang, C.-H. 2019, MNRAS, 490, 3667, doi: [10.1093/mnras/stz2844](https://doi.org/10.1093/mnras/stz2844)
- Zhu, G., Moustakas, J., & Blanton, M. R. 2009, ApJ, 701, 86, doi: [10.1088/0004-637X/701/1/86](https://doi.org/10.1088/0004-637X/701/1/86)